Lone but Not Alone: Precise Positioning of Lone Pairs for the Design of Photocatalytic Architectures

Joseph V. Handy[1] Wasif Zaheer, [1#] Arianna R. M. Rothfuss,[2#] Caitlin R. McGranahan,[2#] George Agbeworvi,[1] Justin L. Andrews,[1] Karoline E. García-Pedraza,[2] John D. Ponis,[1] Jaime R. Ayala,[1] Yu Ding,[3] David F. Watson,[2] and Sarbajit Banerjee[1]**

[1]Department of Chemistry, Department of Materials Science and Engineering, Texas A&M University, College Station, TX 77843 (USA)
[2]Department of Chemistry, University at Buffalo, Buffalo, NY 14260 (USA)
[3]Department of Industrial and Systems Engineering, Texas A&M University, College Station, TX 77843 (USA)
*Corresponding authors: dwatson3@buffalo.edu, banerjee@chem.tamu.edu
[#]These authors contributed equally.

Abstract

With current economic growth and consumption trends projected to bring about a precipitous and rapid rise of the global temperature, the world stands at a crossroads with regards to climate change. The rate at which greenhouse gas emissions from fossil fuels, industry, and land-use is curtailed over the next decade will determine the trajectory of global warming for the rest of the century. It is increasingly apparent that far-reaching decarbonization of the transportation infrastructure will need to be supplemented by extensive carbon capture, storage, and utilization. Taking a leaf from Nature's playbook, photocatalytic architectures that can utilize water and/or CO_2 in conjunction with energy harvested from sunlight and store it in the form of energy-dense chemical bonds represent an attractive proposition. Harnessing solar irradiance, through solar energy conversion involving photovoltaics as well as the photocatalytic generation of solar fuels, and the photocatalytic reduction of CO_2 have emerged as urgent imperatives for the energy transition. Functional photocatalysts must be capable of efficiently absorbing sunlight, effectively separating electron—hole pairs, and ensuring they are delivered at appropriate potentials to catalytic sites to mediate redox reactions. Such photocatalytic architectures must further direct redox events down specific pathways to yield desired products, and ensure the transport of reactants between catalytic sites; all with high efficiency and minimal degradation. In this perspective article, we describe a palette of heterostructures designed to promote robust and efficient direct solar-driven water splitting and CO_2 reduction. The heterostructures comprise $M_xV_2O_5$ or $M_xM'_yV_2O_5$ (where M is a p-block cation, M′ is an s-, p-, or d- block cation) and V_2O_5 represents one of multiple polymorphs of this composition interfaced with semiconductor quantum dots (QDs, binary or ternary II-VI or III-V QDs). The stereochemically active $5/6s^2$ electron lone pairs of p-block cations in $M_xV_2O_5$ give rise to filled mid-gap electronic states that reside above the O 2p-derived valence band. Within heterostructures, the photoexcitation of QDs results in the transfer of holes to the mid-gap states of $M_xV_2O_5$ or $M_xM'_yV_2O_5$ on sub-picosecond time scales. Ultrafast charge separation minimizes the photoanodic corrosion of QDs, which has historically been a major impediment to their use in photocatalysis, and enables charge transport and the subsequent redox reactions underpinning photocatalysis to compete with electron-hole

recombination. The energy positioning and dispersion of lone pair states is tunable through multiple chemical and compositional levers accessible across the palette of $M_xV_2O_5$ or $M_xM'_yV_2O_5$ compounds: choice of lone-pair cation *M* and its stoichiometry *x*, atomic connectivity of V_2O_5 polymorphs, co-intercalation of *M′* cations in "quaternary" vanadium oxide bronzes, anionic substitution; and alternative lone pair vanadate frameworks with altogether different compositions and lattice structures. Design principles for understanding the nature of lone pair states are discussed with reference to hard X-ray photoemission, crystal orbital Hamiltonian population analyses, and spectroelectrochemical signatures. The dimensions, composition, and doping of QDs along with interfacial structure afford additional levers for heterostructure integration, enabling tuning of thermodynamic energy offsets and charge transfer dynamics, which have been systematically optimized across several generations of heterostructures to improve photocatalytic performance. Synthetic strategies to prepare new lone-pair $M_xV_2O_5$ or $M_xM'_yV_2O_5$ compounds and their integration within heterostructures are described. Given the large number of variables, we also discuss prospects for the applicability of machine learning and high-throughput synthesis to tackle high-dimensional materials design problems.

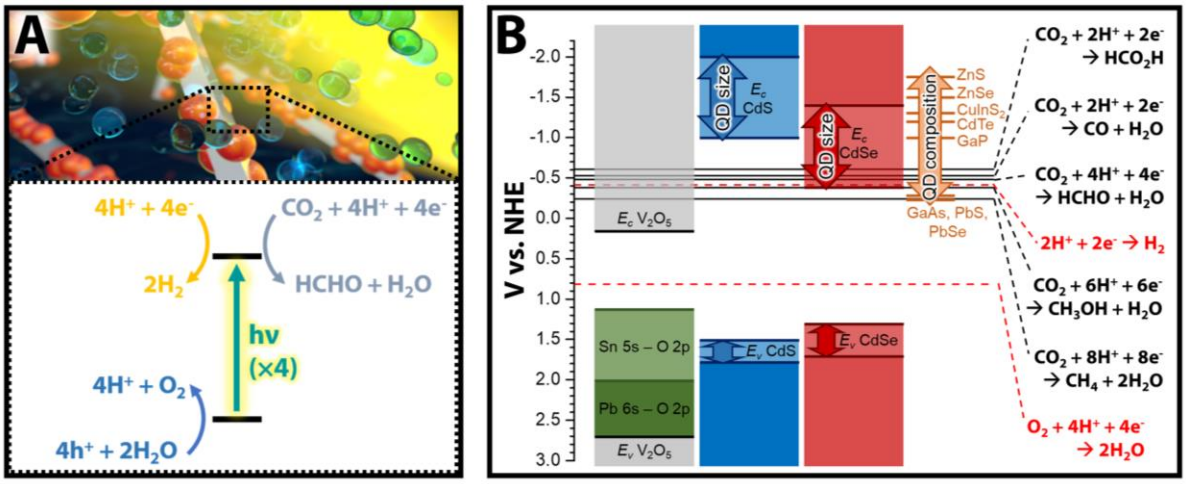

Figure 1. Heterostructures with programmable interfacial energetic offsets driving photocatalysis. (A) Artistic rendering (top) of water-splitting heterostructures comprising $M_xV_2O_5$ nanowires (gray rods) interfaced with QDs (red spheres) under sunlight. Superimposed is a diagram describing photocatalytic water oxidation (blue) coupled with either hydrogen evolution reaction (HER) (yellow) or CO_2 reduction (depicted here as yielding formaldehyde) (gray) using a heterostructured photocatalyst. **(B)** Energy-level diagram highlighting tunable offsets, as a function of composition and size of QDs and composition of $M_xV_2O_5$ (with M = Sn, Pb as representative examples), which drive charge separation and enable control over the thermodynamics of HER, CO_2-reduction, and H_2O oxidation, with the energy levels corresponding to a selection of relevant reactions shown on the right. The background of panel **A** is adapted with permission from reference (22). Copyright 2019 American Chemical Society.

1. Introduction

The reliance of our interconnected global economies on the combustion of fossil fuels has caused myriad and catastrophic environmental, public-health, economic, and geopolitical impacts. With current economic growth and consumption trends projected to bring about a 4°C rise of global temperature by 2100, increasingly frequent extreme weather events, a fractious public policy response, and a limited range of negative emission technologies deployable at scale, the world stands at a crossroads with regards to climate change.[1,2] Afforestation and changes in agricultural practices alone will not be sufficient to keep global warming below the ambitious 1.5°C target of the Paris climate agreement. Instead, a many-pronged approach is required, which must include the development of robust technologies for harnessing solar irradiance, both through solar energy conversion involving photovoltaics and the photocatalytic production of solar fuels, and through the photocatalytic reduction of CO_2. The International Panel on Climate Change estimates that renewables must provide half to two-thirds of energy by 2050, with solar playing a major role, and that cumulative carbon capture needed by 2100 will range from 348 Gt CO_2, under early decarbonization, to 1218 Gt CO_2 if energy-intensive economies continue to grow at an unfettered pace.[3]

Photovoltaics cannot be the only strategy for solar energy conversion; variable insolation necessitates the storage of solar energy, ideally in energy-dense chemical bonds.[4–6] Two promising approaches to solar-to-chemical energy conversion involve water splitting, or the disproportionation of H_2O into O_2 and H_2 (a carbon-free fuel); and, taking a leaf from Nature's playbook, the reduction of CO_2 to fuels such as methane or methanol. The molecular products of CO_2 reduction, hydrocarbons and oxygenates, can be used as carbon-neutral fuels or precursors of chemicals and plastics,[7–12] enabling removal of up to 2.2 Gt CO_2 equivalents per annum and mitigating the need to extract fossil fuels.[13] Water splitting and the photocatalytic reduction of CO_2 are mechanistically similar and have in common stringent requirements in thermodynamics and kinetics. Water splitting involves the concerted transfer of four electrons and four protons at sufficiently reducing and oxidizing potentials, respectively (**Fig. 1A**). Photocatalytic reduction of CO_2 in aqueous media likewise involves multiple proton-coupled electron transfer reactions at appropriate potentials and is further complicated by the potentially broad distribution of CO_2-reduction products (**Fig. 1B**).

Photocatalysts must promote a complex and interconnected progression of reactions and transport processes: (1) absorption of sunlight, (2) separation of electrons and holes, (3) charge transport to catalytic sites, (4) catalyzed redox events directed down specific pathways to yield desired products, and (5) transport of reactants between catalytic sites.[7,14,15] For a given photocatalytic mechanism, it is unlikely that a single material can orchestrate the entire sequence in a synchronized manner; instead, a promising approach is to develop heterostructures comprising multiple components that each mediate a subset of the required processes. Precisely programming cascades of events to split water or to convert CO_2 to fuels, at heterostructures, requires control of (a) thermodynamic driving forces through alignment of energetic offsets such that electrons and holes are delivered to catalytic sites at correct potentials to initiate the reduction of H^+ or CO_2 and the oxidation of H_2O; (b) interfacial charge transfer kinetics enabling charge separation and delivery of long-lived electrons and holes to catalytic sites, which must outcompete recombination and deleterious reactions such as photoanodic corrosion of the catalyst itself; and (c) reaction kinetics at interfaces to drive redox catalysis as close to thermodynamic potentials as possible, enabling effective proton-coupled electron transfer and predictive product selectivity.[4,5,14,15]

We describe here a palette of heterostructures designed to address these challenges and to promote robust and efficient direct solar-driven water splitting and CO_2 reduction. The heterostructures consist of $M_xV_2O_5$ or $M_xM'_yV_2O_5$ (where M is a p-block cation, M′ is an s-, p-, or d- block cation, *x* and *y* are their respective stoichiometries, and V_2O_5 represents one of multiple polymorphs of this composition)[6,16–18] interfaced with semiconductor quantum dots (QDs, binary or ternary II—VI or III—V QDs) (Fig. 1b). The stereoactive $5/6s^2$ lone pairs of p-block cations in $M_xV_2O_5$ give rise to mid-gap electronic states. Within heterostructures, the photoexcitation of QDs results in the transfer of holes to the mid-gap states of $M_xV_2O_5$ or $M_xM'_yV_2O_5$ on sub-picosecond time scales.[19–22] Ultrafast charge separation minimizes the photoanodic corrosion of QDs, which has historically precluded their use in photocatalysis,[15,23,24] and enables charge transport and the subsequent redox reactions underpinning photocatalysis to compete with electron-hole recombination.

Energies and densities of the intercalative mid-gap states of $M_xV_2O_5$ and $M_xM'_yV_2O_5$ can be modulated with composition (selecting from different p-block cations with stereochemically active lone pairs for M and s/p/d-block cations for co-intercalated M′), atom configuration (atomic connectivity of different V_2O_5 polymorphs and the specific interstitial sites occupied by M and M′ cations), and electronic structure, enabling control over the driving forces of interfacial charge transfer and catalytic oxidation reactions.[6,19–22,25] Likewise, the energies of photoexcited electrons in QDs are tunable using size, composition, surface functionalization, and alloying, enabling control over driving forces of QD-mediated reduction reactions in $M_xV_2O_5$/QD and related heterostructures (**Fig. 1B**). As indicated in **Fig. 1B**, modulating the size of QDs principally influences the energy positoning of the conduction band edge,[26,27] whereas composition (and especially choice of anion) chiefly determines energetic positioning of the valence band, facilitating overlap with $M_xV_2O_5$. A smaller extent of tunability, ca. 100 meV, can be accessed through choice of ligand.[28] This class of heterostructure photocatalysts thus offers unusual, and perhaps unprecedented, tunability of the thermodynamics and kinetics of excited-state charge transfer processes underpinning the photocatalytic production of solar fuels.

Several generations of $M_xV_2O_5$/QD heterostructures have been designed and characterized in terms of their electronic structure, excited-state charge transfer dynamics, and performance in photocatalytic proton reduction.[6,19,21,22,25,29,30] By developing high-throughput topochemical synthetic methods, we have recently prepared and characterized a palette of new ternary $M_xV_2O_5$ and quaternary $M_xM'_yV_2O_5$ compounds with composition- and structure-dependent electronic properties, which are ripe for incorporation into heterostructure photocatalysts. This perspective article summarizes the distinctive electronic structure of $M_xV_2O_5$/QD heterostructures, highlights the potential to control both the thermodynamics and kinetics of excited-state charge-transfer processes central to photocatalysis, provides an overview of synthetic strategies, and addresses future prospects for the heterostructure photocatalysts. We describe the electronic structure of $M_xV_2O_5$ and $M_xM'_yV_2O_5$ compounds and the advantages of lone pair-derived mid-gap states, relative to band-edge states, in photocatalysis. We explain how the energy and distribution of mid-gap states of $M_xV_2O_5$ and $M_xM'_yV_2O_5$ compounds can be tuned with the polymorph of the V_2O_5 framework and the identity and properties of intercalated cations, and we highlight lone-pair vanadates beyond $M_xV_2O_5$ and $M_xM'_yV_2O_5$ that are possible candidates for similar photocatalytic architectures. Synthetic strategies to $M_xV_2O_5$/QD and related heterostructures are described. The influence of interfacial electronic structure on excited-state charge transfer, the key charge-separation event in photocatalysis, is discussed, along with an overview of photocatalytic performance of $M_xV_2O_5$/QD heterostructures. Finally, we address prospects and challenges

pertaining to improved navigation of the vast design space involving lone-pair oxides, as well as to expanding the scope of photocatalytic reactions promoted by the heterostructures.

2. Revised Lone Pair Model and the Origin of Lone Pair States

The filled *s*-subshells of post-transition-metal cations with an $(n-1)d^{10}ns^2np^0$ electronic configuration oftentimes exhibits properties of stereochemically active electron pairs by repelling adjacent bonding pairs to induce structural distortions around the metal center, the magnitude of which depends strongly on the nature of anion interactions.[31] The electron lone pairs occupy a volume that is equivalent to a fluoride or oxide anion, and can induce a considerable off-centering of the metal from the centroid of its polyhedron.[32] While initial studies assumed that the lone pairs were predominantly nonbonding in nature, there is considerable evidence now that whether the lone pairs are "inert" or stereochemically active depends in large measure on their hybridization with anions, as captured in the revised lone pair model by Walsh *et al.* (**Fig. 2**). The presence of lone-pair repulsions can induce oriented dipoles that trigger deviations from centrosymmetry across the crystal structure. Such deviations have been exploited to design piezoelectric, ferroelectric, and nonlinear optical materials exhibiting a second-harmonic generation response and render stereoactive lone pairs an important design principle for modulating lattice symmetry.[33] The lattice anharmonicity introduced by the Pb $6s^2$ electron lone pairs has further been shown to induce a metal—insulator transition in β-$Pb_{0.33}V_2O_5$, and by Macaluso and co-workers to underpin a reversible thermochromic transition in $PbVO_3Cl$.[34–36] In $CsSnBr_3$, emergent asymmetry is observed that is ascribed to Sn^{2+} lone-pair-derived stereochemical activity upon warming, a phenomenon the authors have labeled "*emphanisis*".[37] Anomalies in thermal expansion coefficient and the emergence of an unusual pseudo-symmetry is further mediated in part by the stereochemical activity of Pb^{2+} lone pairs in $HC(NH_2)_2PbI_3$.[38] Moreover, the Sb $5s^2$ stereoactive electron lone pairs have been shown to facilitate reversible fluoride-ion insertion in $FeSb_2O_4$ at room temperature by weakening iron—fluorine interactions, thereby further providing a design principle for insertion electrodes of anion batteries.[39,40]

The energy positioning of stereochemically active electron lone pairs is tunable across an energy range of interest for enabling hole extraction from II-VI and III-V QDs in photocatalytic heterostructures, as demonstrated for β-$Pb_{0.33}V_2O_5$/QD and β-$Sn_{0.23}V_2O_5$/QD heterostructures.[19–21] **Figures 2A—C** depict visualizations of the electron lone pairs in β-$Pb_{0.33}V_2O_5$, $PbVO_3Cl$, and $FeSb_2O_4$ as calculated by electron localization function analysis. Historically, lone pairs derived from p-block cations were presumed to be nonbonding in nature but their role in affecting structural distortions depending on their specific anion coordination environment challenged this notion. Hybridization of the lone pair ns^2-states with ligand *p* states is stabilized by a second-order Jahn—Teller distortion.[41,42] The link between lone-pair—anion interactions and local structural distortions can be elucidated by delineating orbital contributions through energy-variant photoemission spectroscopy, which in conjunction with density functional theory calculations has led to the postulation of the revised lone pair model.[41,42] As per this model, the hybridization of cationic 5*s* or 6*s* lone pair states with filled anion 2*p* or 3*p* states yields a combination of occupied bonding and anti-bonding lone-pair—anion states. The latter is further stabilized by mixing with unoccupied cation 5*p* and 6*p*-states, yielding an occupied antibonding "mid-gap" state above the anionic *p* states in the valence band with a spectroscopic signature distinguishable using hard X-ray photoemission spectroscopy (HAXPES).[43] **Figure 2G** shows the relative energetics of lone pair states and anion *p* states; their energetic proximity determines the strength of hybridization and the resulting stabilization of anti-bonding states at the top of the valence band. Crystal orbital

Hamilton population (COHP) analyses are furthermore effective in delineating the energy positioning and the pairwise bonding/antibonding character of the electron lone pair states resulting from the interaction of electron lone pairs of p-block cations with the anionic *p* states (**Figs. 2D—F**).

3. Lone-Pair-Derived Electronic States and Photocatalysis

The extent of hybridization between the lone-pair-derived *n*s-states with ligand *p* states and the relative stability of lone pair-derived mid-gap states is dictated by the choice of both the post-

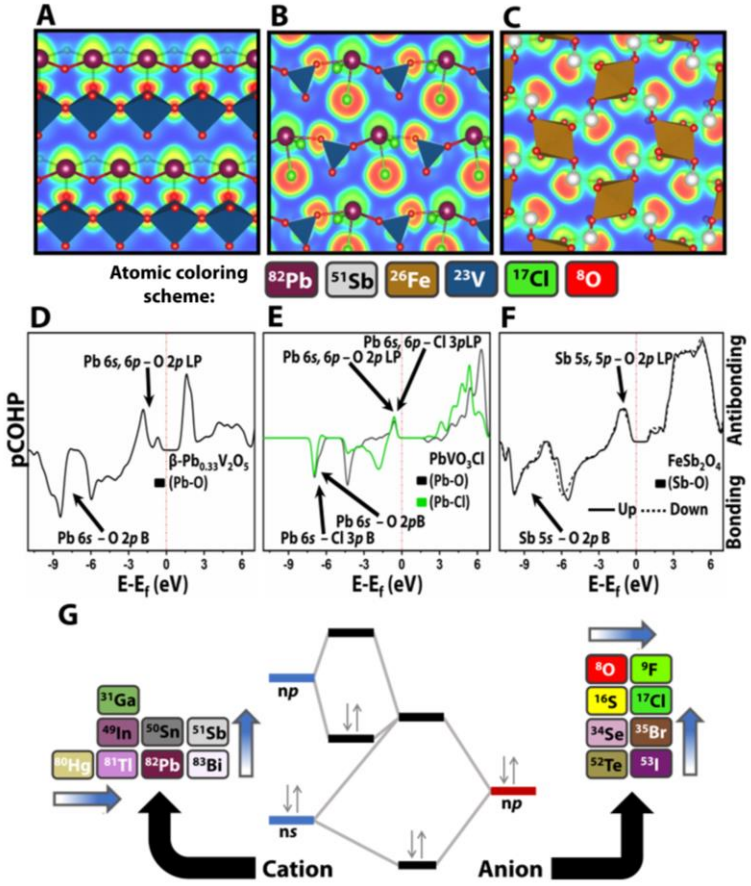

Figure 2. Visualizing Stereoactive Electron Lone Pairs using Electron Localization Function (ELF) and Crystal Orbital Hamilton Population (COHP) Analyses (A) ELF sliced along the (001) plane of β-$Pb_{0.33}V_2O_5$. **(B)** ELF sliced along the (100) plane of $PbVO_3Cl$. **(C)** ELF sliced along (001) plane of $FeSb_2O_4$, with color scheme for atoms in these structures shown below the panels. COHP analyses plot for **(D)** Pb—O interactions in β-$Pb_{0.33}V_2O_5$; **(E)** Pb—O and Pb—Cl interactions in $PbVO_3Cl$; and **(F)** Sb—O interactions in $FeSb_2O_4$. COHP Interactions are plotted such that the bonding interactions between two species are negative on the vertical axis, whereas the antibonding interactions are positive on the vertical axis. **(G)** Molecular orbital representation showing the lone pair states derived from the hybridization of cationic n*s* and n*p* states with the anionic n*p* states, with blue arrows indicating an *increase* in the binding energy for cationic *n*s and anionic *n*p orbitals as one moves across the periodic table. Panel **(F)** is adapted from reference (40). Licensed under CC BY-NC-ND 4.0 / data reproduced and relabeled from original.

transition-metal cation and *p*-block anion, the stoichiometry of the cation relative to the anion, and the atomic connectivity as defined by the crystal structure of the compound. The lone-pair-derived mid-gap states in post-transition metal oxides can be tuned (along with their conduction and valence band edges) to design photocatalytic architectures with electronic structures that are matched with redox potentials suitable for water splitting (**Fig. 1B**).

The oxides of Sn (SnO, SnO_2, and Sn_3O_4) present an interesting case study highlighting the role of lone pair-derived mid-gap states in reducing thermodynamic offsets for the photoelectrochemical splitting of water. SnO_2 is a wide-bandgap (ca. 3.6 eV) semiconductor,[44] where Sn is fully oxidized to Sn^{4+} and the Sn 5*s*^{0} states are present at the conduction band minimum (CBM), more positive than the hydrogen evolution potential, which makes it an inefficient catalyst for photoelectrochemical hydrogen evolution. In contrast, SnO has a narrow indirect bandgap of ca. 0.7 eV,[45] where the hybridization of 5s^2 electron lone pairs on Sn^{2+} with O 2*p* leads to the formation of lone-pair-derived mid-gap states that push the valence band maximum (VBM) more negative than the hydrogen evolution potential. The misalignment of the band edges with the hydrogen evolution potential, and the less-than-optimal band gaps, render both SnO_2 and SnO unviable for water splitting, as corroborated with experimental studies.[44] However, in Sn_3O_4, the mixed valency of Sn (Sn^{2+} and Sn^{4+}) leads to the formation of sufficient lone-pair-derived mid-gap states such that the VBM is appropriately aligned, and the bandgap is overlapped with the solar spectrum such as to enable the effective photoelectrochemical splitting of water.[44]

$BiVO_4$ presents another case where the stereochemistry of Bi 6*s*^{2} electron lone pairs governs photocatalytic activity. The scheelite structure of $BiVO_4$ exists in monoclinic and tetragonal symmetries with a reversible transition between the two phases. Despite having similar band gaps (2.40 eV for monoclinic and 2.34 eV for tetragonal phase), the monoclinic phase is more photocatalytically active for water splitting. In tetragonal $BiVO_4$, the VBM is primarily O 2*p* in character, whereas the CBM is V 3*d*. The reduced symmetry in the monoclinic phase leads to structural distortions of the Bi—O polyhedron that allow Bi 6*s*^{2} lone pairs to hybridize with O 2*p* states. The hybrid states derived from the Bi 6*s*^{2} electron lone pair lie above the O 2*p* states and push the VBM to a more negative potential with respect to SHE, improving the alignment of VBM with water redox potentials for efficient photocatalysis.[46–48] Oxidative catalysis formally invokes the lone-pair-derived Bi^{3+}/Bi^{5+} states hybridized with O 2p at the mid-gap states, whereas the reductive catalysis involves V^{3+}/V^{2+} at the CBM. However, despite suitable band alignments for charge transfer and an appropriate bandgap for light absorption, the widespread use of monoclinic $BiVO_4$ as a photocatalyst has been stymied by the short hole diffusion length, which leads to facile recombination of photogenerated charge carriers.[49]

As an alternative to singular direct-bandgap post-transition-metal oxide photocatalysts where conduction band and lone-pair-derived valence band states are sought to be aligned with proton reduction and water oxidation potentials, respectively, a different strategy involves the design of heterostructures that leverage lone pair states to affect interfacial charge separation upon photoexcitation. Lone-pair-derived states have been used for hole extraction within photocatalytic heterostructures interfacing compounds such as β-$Pb_xV_2O_5$ and β-$Sn_xV_2O_5$ with II−VI semiconductor quantum dots (QDs) as illustrated in **Figure 1**. Chalcogenide quantum dots (QDs) are ideal light-harvesting elements given their high absorption coefficients; however, their use as photocatalysts has been limited as they suffer from anodic photocorrosion in aqueous media from the localization of photogenerated holes at surface traps.[50] The filled lone pair states of the post-transition metal oxides can accept photoexcited holes from QDs and further transport them to co-catalysts for water splitting. The $M_xV_2O_5$/QD heterostructures present a new class of

photocatalysts where the ionization potential of the lone-pair-derived states of the $M_xV_2O_5$ nanowire near the VBM can be precisely modulated to accept holes from QDs of different compositions and dimensions. This design principle was first demonstrated to create β-$Pb_{0.33}V_2O_5$/CdSe-QD heterostructures as photocatalysts for water splitting.[19,20] The thermodynamic band alignment between the nanowire and the QDs at the valence band was further improved by interfacing β-$Pb_{0.33}V_2O_5$ nanowires with CdS QDs, as well as β-$Sn_{0.23}V_2O_5$ nanowires with CdSe QDs.[19,21] The electronic states derived from the Sn 5*s* electron lone pairs were precisely engineered to extract photogenerated holes from the CdSe QDs at the VB, which led to efficient hydrogen evolution.[21]

The design space of $M_xV_2O_5$ and co-intercalated $M_xM'_yV_2O_5$ family is substantial. The ability to grow single crystals in a high-throughput manner has greatly accelerated materials discovery across numerous vectors of this design space and has afforded precise control over the energy positioning and dispersion of these lone-pair states, rendering them versatile elements in the design of photocatalytic architectures.

3.1. Modulation of Lone Pair States as a Function of Framework Connectivity Across V_2O_5 Polymorphs

The expansive family of intercalated $M_xV_2O_5$ materials is well-suited to lone-pair engineering as a result of the extensive structural diversity of V_2O_5 frameworks. V_2O_5 crystallizes in a multitude of open framework polymorphs with single-/double-layered or tunnel-like extended structures, typically with low-symmetry space groups; multiple crystallographically-distinct vanadium sites are common and give rise to complex Fermi surfaces and considerable scope for tunability of the bandgap.[16,18] The thermodynamically stable polymorph of V_2O_5, α-V_2O_5 shown in **Figure 3A** has a unique vanadium position, and is the starting point for atomic structure (and by extension, electronic structure) modification by the insertion of different cations.[51,52] The abundance of interstitial sites between V_2O_5 galleries, in combination with easy redox between V^{4+}/V^{5+} and V^{3+}/V^{4+} gives rise to many distinct accessible sites, with substantial implications for both atomic and electronic structure. The formation of polaronic V3d electronic states at reduced V sites has significant impact on the positioning of the valence band edge in catalytic structures, and mixed-valence V has been observed to facilitate the transport of holes and/or electrons.[20,53] Notably, polaronic filled valence band states can hybridize with closely spaced $5s^2/6s^2$ antibonding lone-pair-derived states.[21] The insertion of guest cations in varying local coordination environments, based on their ionic radius, available valence electrons (oxidation state), and softness/hardness holds scope for modulating the overall electronic structure and charge-transport pathways.[18,54]

One illustrative example is the "tunnel phase" V_2O_5 structure, the empty, fully-oxidized framework of which is represented as (metastable) ζ-V_2O_5.[55] In stoichiometries of ca. $0<x<0.33$, this structure hosts guest cations in the crystallographic β site, with relatively small cations (e.g., Li^+ in β-$Li_{0.33}V_2O_5$) assuming a 5-fold coordination geometry and larger metal ions (e.g., Pb^{2+} in and β-$Pb_{0.3}V_2O_5$) assuming a highly distorted 7-fold coordination geometry (**Fig. 3A**). For $0.33<x<0.66$, a 5-coordinate β' position is instead favored for smaller cations, with β'-$Cu_{0.5}V_2O_5$ (Fig. 3A) further exhibiting a split-site disorder at this position, the oscillation of which gives rise to polaron destabilization at high temperature, inducing a strong metal—insulator transition (larger cations tend to be limited to a stoichiometry of ca. 0.33 for this framework).[56] When subjected to

a large driving force for intercalation, an entire continuum of crystallographic sites including an unusual 2-coordinate position have been identified in ζ-V_2O_5 to accommodate Li-ions, with the extended V_2O_5 framework exhibiting remarkable durability across multiple transformations.[57] The removal and insertion of different guest cations while leaving the overall V_2O_5 framework intact then allows for exploration of metastable V_2O_5 phase space and distorted empty structures as hosts for the insertion of lone-pair cations with many interstices available for site-selective positioning.[58] Using these methods to achieve different V_2O_5 connectivity therefore provides a primary means for band structure engineering, by creating a valence band principally of V 3*d*[1] bonding states

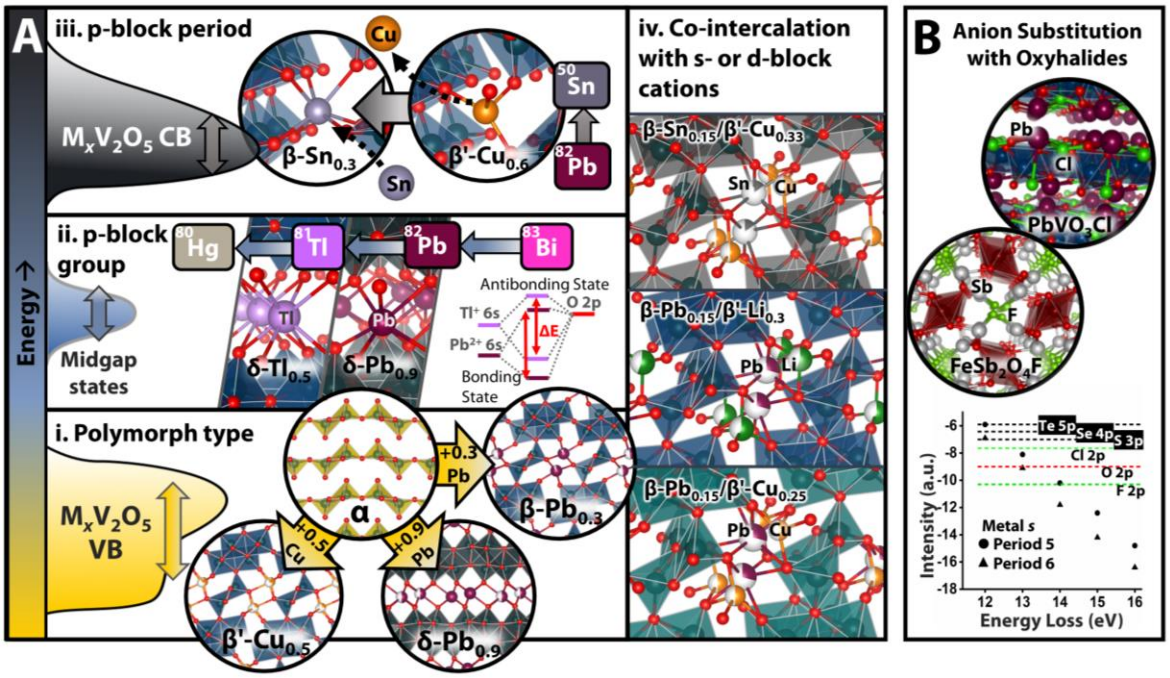

Figure 3. Compositional and Structural Levers for Modulating the Energy Positioning and Dispersion of Lone-Pair States (A) Overview of available chemical levers for modulating the electronic structure of lone-pair $M_xV_2O_5$ bronzes with a view towards optimizing energetic offsets with QDs to promote effective charge separation and with water redox potentials to ensure delivery of electrons and holes at low overpotentials. The left schematic represents the band structure of $M_xV_2O_5$. The energy positioning and dispersion of midgap states is tunable as a function of (i) polymorph type, which is represented by a selection of V_2O_5 structures, including the thermodynamic minimum α-V_2O_5, and different tunnel- and layer-like polymorphs accessible by the insertion of differing stoichiometries of Cu and Pb; (ii) Group of the inserted p-block cation, comparing the crystal structures and cation coordination environments of δ-$Pb_{0.9}V_2O_5$ and δ-$Tl_{0.5}V_2O_5$, respectively, with the impact of p-block 6*s* and O 2*p* hybridization on molecular orbital energetics sketched on the right-hand side of the panel; (iii) Period of the inserted p-block cation, which can be modulated by approaches such as the topochemical removal of Cu-ions from a β'-site and insertion of Sn-ions to the β-site; (iv) Co-intercalation with s-, p-, or d-block cations, which cover a potentially vast array of new structures, three recently discovered structures grown as single crystals are shown: β-$Pb_{0.15}$/β'-$Li_{0.3}V_2O_5$, β-$Sn_{0.15}$/β'-$Cu_{0.33}V_2O_5$, and β-$Pb_{0.15}$/β'-$Cu_{0.25}V_2O_5$. **(B)** Structures of mixed anion compounds–halide substitution on the oxide lattice holds promise for precise modulation of stabilization of anti-bonding lone pair states and thus the energy positioning and dispersion of midgap states. Below is a plot comparing the relative energetics of relevant of p-block cationic-*s* and anionic-*p* states.

dispersed by anisotropic symmetry and multiple coordination environments of edge- or corner-sharing tetrahedra, square pyramids, and octahedra.

3.2. Compositional Levers for Lone Pair Engineering

These atomistic design features—namely, diversity of polymorph, multiplicity of available interstices, and ready accessibility of removal and insertion of new cations—make $M_xV_2O_5$ and $M_xM'_yV_2O_5$ compounds an excellent platform for the precise positioning of lone-pair states.[54,58–61] Available "levers" for modifying the band structure by precise positioning of lone-pair states as a function of atomic species and bond connectivity are outlined in Figure 3: i) polymorph type; ii) periodic group of inserted p-block cation, iii) period of inserted p-block cation; and iv) co-intercalation with s-, p-, or d-block cations. As introduced in **Section 3.1**, a first available knob for modifying band structure in this family of materials (with broad contours of electronic structure features sketched along an energy axis on the left-hand side of **Fig. 3**) is selection of polymorph type; choice of one- and two-dimensional extended V_2O_5 structures (synthetically templated by choice of guest cations in hydrothermal synthesis or melt growth). The representative 1-D structure discussed here is the β-$M_xV_2O_5$ family of bronzes, where corner-sharing double-layers of VO_6 octahedra are joined by "walls" of VO_5 square pyramids to form tunnels (the structures of β'-$Cu_{0.5}V_2O_5$ and β-$Pb_{0.3}V_2O_5$ as elucidated from single-crystal X-ray diffraction are shown in **Figures 3A-i**). The 2D structures are mainly of the δ-$M_xV_2O_5$ family where condensed double-layers of VO_6 octahedra form infinite sheets that are filled in by the inserted cation *M* (an example structure of δ-$Pb_{0.9}V_2O_5$, which is close to the intercalation limit for this structure, is shown in **Figure 3A-i**). For Pb^{2+} and Sn^{2+} cations, which are of particular interest for photocatalytic architectures, the limit of intercalation in the β-$M_xV_2O_5$ structure, whether accessed thermodynamically or topochemically (in the case of Pb^{2+} and Sn^{+} insertion, respectively) is approximately x = 0.33, when exactly ½ of the β-sites in the tunnel are filled. Above these stoichiometries, in thermodynamic structures accessed by direct synthesis, the host framework will adopt a layered δ-$M_xV_2O_5$ stoichiometry, which can incorporate these lone-pair guest cations up to roughly x = 1, representing a widely tunable range of stoichiometries. Partial deintercalation or direct synthesis in stoichiometric amounts can be achieved to vary the $Pb^{2+}/Sn^{2+}/Tl^{+}$ content in these double layered δ-phase structures. Beyond δ-$M_xV_2O_5$, many related 2D structures are also known with varying configurations and stacking sequences of condensed double-layered $[V_4O_{10}]$ slabs including ε-$Cu_xV_2O_5$[52,62] and transition-metal solvates of the formulas δ-$M_{0.25}V_2O_5{\cdot}zH_2O$ and σ-$M_{0.25}V_2O_5{\cdot}zH_2O$ (two of which are shown as crystal ensembles in **Fig. 4**, with the crystal structure of the Ni hydrate illustrated in **Fig. 4D**).[63,64] These other polymorphs exhibit similar compositional diversity and are further amenable to topochemical transformations.

Hybridization of p-block lone-pair states with O 2p orbitals creates hybrid antibonding states that contribute to the mid-gap states lying above the valence band maximum (**Figure 3A-ii**).[35] For lone-pair engineering in these host structures, the choice of p-block cation in both structural types is of crucial importance as a means of selecting the dispersion and the energy positioning of 5s and 6s lone-pair states added to the top of the valence band as "mid-gap" states. The choice of p-block cation also influences the hybridization of V 3d states; as an example, the

crystal structures of δ-$Tl_{0.5}V_2O_5$ and δ-$Pb_{0.9}V_2O_5$ derived from single-crystal X-ray diffraction are shown adjacent to one another in Figure 3A-ii to highlight the variation in local coordination, with Pb^{2+} adopting a distorted 7-fold coordination and Tl^+ adopting a cubic 8-fold coordination. Notably, the ordering of the lone-pair cations further dictates the pattern of electron localization on the V_2O_5 framework, which has implications for hole/electron transport. Temperature-dependent Mott transitions, polaron localization, and spin ordering have been observed in δ-$M_xV_2O_5$ bronzes as a result of cation reordering.[65,66] The energy positioning of mid-gap states increases from left to right in going from Bi^{3+} to Tl^+. The Hg_2^{2+} dimers imbue a somewhat more complex electronic structure: $6s^2$ contributions from the Hg_2^{2+} dimers show some similarities to lone-pair contributions in terms of hybridization of s-states with O 2*p* orbitals, which is evidenced in HAXPES as an amplification of intensity at high excitation energies and a slight asymmetry around the dimers; however, further studies are needed to fully distinguish the contribution of 6*s* states to bonding of the dimers in this framework, which has long been a challenging problem for density functional theory treatments.[67]

The identity of the p-block ion provides a powerful means of modulating the energetic positioning of lone-pair-derived states, e.g., Sn^{2+} instead of Pb^{2+}. This is exemplified in the case of the tunnel-like β/β'-$M_xV_2O_5$ framework in Figure 3A-iii. Placement of Sn^{2+} ions (and corresponding 5*s* lone-pair states) within the tunnel must be achieved by the topochemical removal of Cu^+ ions and insertion of Sn^{2+} at low (<400°C) temperatures, as the β-$Sn_{0.3}V_2O_5$ structure lies outside the thermodynamic minimum at these stoichiometries. Topochemically targeting for Sn lone-pair states in this way raised the energy of the midgap states, enabling effective overlap with the VBM of CdS and CdSe QDs and thus enabling a substantial improvement in the interfacial energetic offsets driving charge separation and photocatalytic performance of QD-containing heterostructures.[21] The use of topochemistry to combine V_2O_5 host structures with select p-block cations represents a versatile strategy in the design of new structures with precisely positioned electronic states for hole extraction.[17]

3.3. co-Intercalation as a Means of Lone Pair Engineering

A further method for adjusting the electronic character of lone-pair V_2O_5 bronzes, namely co-intercalating multiple cations with highly selective site preferences, has recently been developed and is a direct result of the plethora of insertion sites available in the ζ-V_2O_5 tunnel. While a disordered layered "quaternary" τ-$(Ag,Cu)_{0.92}V_2O_5$ bronze has been investigated previously,[68] the deliberate co-intercalation of site-selective cations within tunnel-type V_2O_5 bronzes represents a new and entirely unexplored vector for electronic structure modulation. This approach presents combinatorial opportunities for site-selective cation mixing and valence band engineering in the solid state, with a wide range of structures accessible by diverse synthetic routes. **Figure 3A-iv** displays three new quaternary $M_xM'_yV_2O_5$ structures that take advantage of the relative site preferences of different cations in order to modify the existing electronic properties of the ternary lone-pair bronze via hybridization with an s- or d-block co-intercalant. Subtle structural distortions introduced by the inclusion of secondary intercalants can have substantive long-range effects owing to changes in electron (de)localization and orbital hybridization. β-Pb_x/β'-$Cu_yV_2O_5$ has been synthesized, along a range of Pb and Cu stoichiometries *x* and *y* as per:

$$\alpha\text{-}V_2O_5\ (s) + x PbC_2O_4\ (s) + y Cu\ (s) \rightarrow \beta\text{-}Pb_x/\beta'\text{-}Cu_yV_2O_5\ (s) + 2xCO_2\ (g) \quad (1)$$

by mixing Cu metal, PbC_2O_4, and α-V_2O_5 powders, and annealing under Ar at 550° for 24 h. Large single-crystals of β-Pb_x/β'-$Cu_yV_2O_5$ have been obtained by melting the product powder at 800°C in sealed quartz ampoules under vacuum and slowly cooling at a rate of 2°C/h. Single-crystal X-ray diffraction confirms an atomic crystal structure wherein Pb^{2+} cations prefer a 7-coordinate β-site occupancy and Cu^+ cations prefer a 5-coordinate β'-site occupancy. Topochemical lithiation of pristine β-$Pb_{0.3}V_2O_5$ with *n*-butyllithium yields a similar product structure where Li^+ ions are selectively inserted to the β'-site as per:

$$\beta\text{-}Pb_{0.3}V_2O_5\ (s) + x\ n\text{-}LiC_4H_9\ (\text{heptanes}) \rightarrow \beta\text{-}Pb_{0.3}/\beta'\text{-}Li_xV_2O_5\ (s) + x/2C_8H_{18}\ (\text{heptanes}) \quad (2)$$

β-Sn_x/β'-$Cu_yV_2O_5$ has likewise been accessed by mixing powders of β'-$Cu_xV_2O_5$ with SnC_2O_4 in a hexane slurry, followed by annealing under Ar flow at 350°C to effect the topochemical insertion of Sn^{2+} to the pre-intercalated β'-$Cu_yV_2O_5$ tunnels as per:

$$xSnC_2O_4\ (s) + \beta'\text{-}Cu_yV_2O_5\ (s) \rightarrow \beta\text{-}Sn_x/\beta'\text{-}Cu_yV_2O_5\ (s) + 2CO_2\ (g) \quad (3)$$

In the case of β-Pb_x/β'-$Cu_yV_2O_5$, resonant elastic/inelastic X-ray Scattering (REIXS) experiments indicate substantial amplification of vanadium L-edge d—d charge transfer features with increasing co-intercalation. Co-intercalation, especially site-selective modification, thus affords a large library of $M_xM'_yV_2O_5$ compounds with considerable scope for modification of the electronic structure of lone-pair bronzes to improve thermodynamic energy offsets in heterostructures, control electron and hole carrier concentrations, and mediate relaxation pathways for photoexcited heterostructures. Furthermore, co-intercalation provides a straightforward means of disentangling electronic contributions from the lone-pair cation with V3*d* contributions arising from mixed vanadium valence; as for a given lone-pair cation stoichiometry *x*, the ratio of V^{4+}/V^{5+} can be adjusted independently with co-intercalant stoichiometry *y* using *s*- or *d*-block intercalants. Ongoing work is focused on teasing out the optimal combination of mid-gap lone-pair states and vanadium reduction that allows for desired energy offsets and band dispersion while facilitating facile hole transport away from the QD interface. A foundry of over 100 distinct compounds characterized by single-crystal diffraction has become available as illustrated in **Figure 4A**. To emphasize the sheer variety possible in the chemical modulation of vanadium oxide structures, we also include a depiction of the unusual solvated structure $(TMA)_4H_2V_{10}O_{28}(CH_3COOH)(H_2O)_{2.8}$ (TMA = tetramethylammonium; large crystals of this species are shown in **Figure 4A** and a view of the crystal structure is shown in **Figure 4B**). This little-explored structure, which can be accessed via mild hydrothermal methods,[69] consists of $[H_2V_{10}O_{28}]^{4-}$ clusters entirely surrounded by solvent molecules, effectively representing a "0-dimensional" vanadium oxide structure; the unusual structural motif suggests solvent replacement and solvent co-intercalation as an additional potential vector for chemical modification. The crystal structure of hydrated δ-$(Ni{\bullet}H_2O)_xV_2O_5$ is shown in **Figure 4D**, illustrating an additional structural motif accessible in solvated vanadium oxide bronzes.[63]

3.4. Lone Pairs in Ternary and Quaternary Vanadates

Ternary and quaternary vanadates exhibit considerable compositional and structural diversity by dint of the multiple available redox states of vanadium and accessibility of tetrahedral, square pyramidal, and octahedral local coordination environments.[70–74] In addition to intercalation of p-block cations in one of many V_2O_5 polymorphs, other structural motifs are available such as layered trivanadates (V_3O_8).[75,76] However, in comparison to $M_xV_2O_5$ systems, the structure and

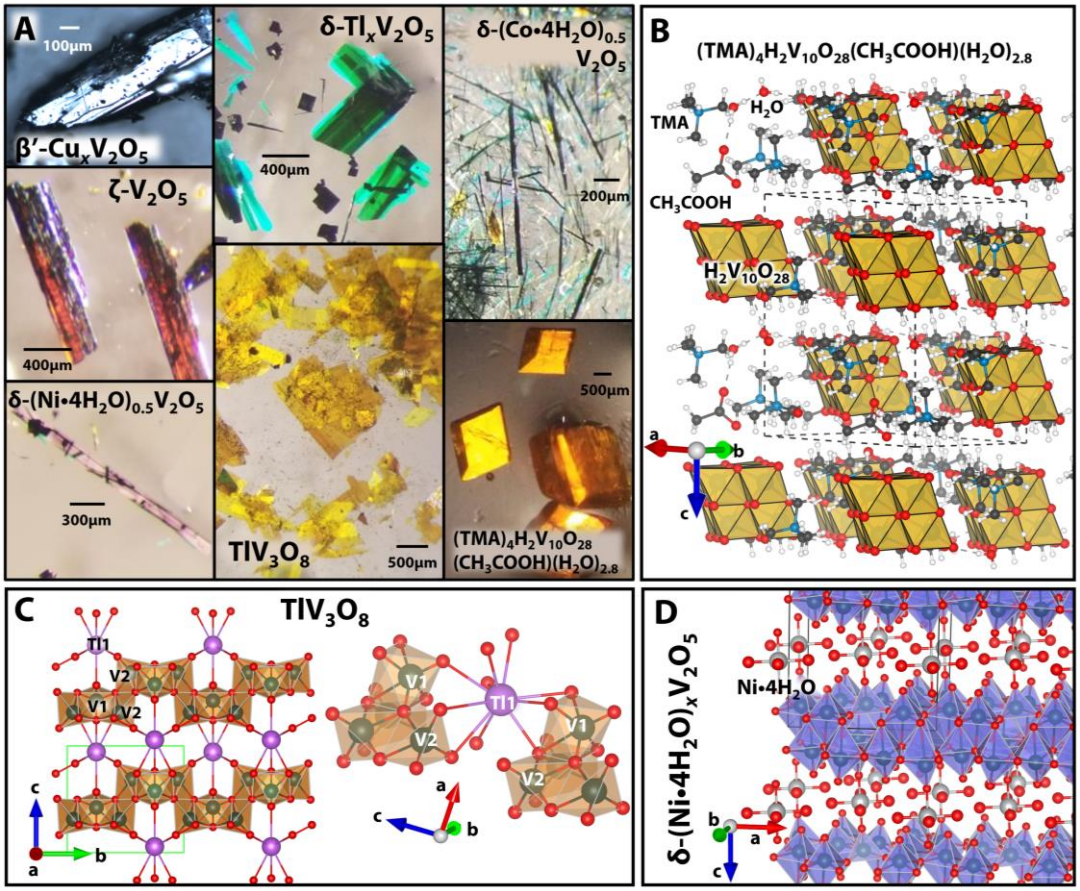

Figure 4. "Crystal Foundry" and Selected Vanadate Crystal Structures. (A) A selection of digital photographs highlighting the diversity of stable and metastable vanadates accessible as large single-crystals, with great variety in morphology, cation- and solvent-intercalation, and optical appearance. **(B)** View of the triclinic $(TMA)_4H_2V_{10}O_{28}(CH_3COOH)(H_2O)_{2.8}$ (TMA = tetramethylammonium) crystal structure viewed down the (110) axis, showing how the structure is formed by a lattice of discrete $H_2V_{10}O_{28}$ clusters bridged in all directions by a combination of incorporated H_2O, CH_3COOH, and TMA moieties. Unit cell boundaries are indicated by dashed lines. **(C)** View of the layered TlV_3O_8 structure (left-hand side), viewed down the *a*-axis, with the unique Tl and V atoms labeled; unit cell boundaries are indicated by a green line; and local view of the distorted 10-fold Tl coordination environment (right-hand side), with atomic labels shown for the Tl atom and two unique V atoms that are bridged by oxygen atoms. **(D)** Perspective view of the layered δ-$(Ni•4H_2O)_xV_2O_5$ structure, viewed down the *b*-axis, showing V_2O_5 layers filled by Ni atoms coordinated to water oxygens (shown as larger red spheres, H atoms omitted for clarity) in a square planar arrangement. Atomic coloring scheme: Red = O, Black = C; Blue = N, White = H; Teal = V, Purple = Tl, Gray = Ni; V—O polyhedra colored gold in panels B and C, and purple in panel D.

properties of *ns* lone-pair trivanadates of the formula MV_3O_8 (M = K, Rb, Cs, Tl)[77,78] remain less explored. As an example, TlV_3O_8 is a layered monoclinic system (space group *P21/m*) containing two distinct vanadium coordination environments (shown in **Figure 4C**). The coordination of the V(1) atom is a strongly distorted octahedron, whereas V(2) is ensconced within a square pyramid. The V(1) ions form an edge-shared square pyramidal network arrayed in a zigzag fashion; the V(2) ions form twisted zigzag chains of edge-shared VO_6 octahedra. The structure is essentially identical to that reported for KV_3O_8, $NH_4V_3O_8$, CsV_3O_8, and RbV_3O_8.[77,78] The magnetic susceptibility of TlV_3O_8 exhibits a ferromagnetic transition at ~140K. Based on determination of the ordered and effective moments, the magnetic transition is derived from superexchange coupling between the oxygen p-orbitals and the reduced V^{n+} centers (V^{n+}-O-V^{n+}) mediated across structural distortions of the local bonding geometries due to the presence of the stereoactive $6s^2$ lone pairs of Tl^+. p-block vanadates thus hold potential for substantial tunability of energy positioning of mid-gap states through variation of structural motifs, as well as for modulating vanadium-derived conduction band edges through different combinations of mixed valent vanadium centers.

3.5. Anion Control of Lone-Pair States

In addition to the structural and compositional levers based on cations, the anionic substitution of oxygen can also be used to fine-tune the energy positioning of the electron lone pair-derived mid-gap states. As shown in **Figure 2**, the relative energetic positioning of anion 2/3p states with respect to lone-pair-derived 5/$6s^2$ states governs their extent of hybridization and the ultimate energy positioning of the filled anti-bonding states at the top of the valence band. In other words, anion hybridization is key to determining the stereoactive *versus* inert nature of lone pairs.[31,41] Mixed-anion systems such as oxyhalides, oxychalcogenides, and oxypnictides of post-transition metal cations present another means of modulating the position and composition of the mid-gap states.[34,79–81] By modifying the anion hybridizing with the p-block cation, the position and metallic nature of the electronic states derived from stereoactive lone pair electrons can be adjusted. HAXPES analysis of a mixed-anion system ($PbVO_3Cl$) has shown that in addition to the Pb-O hybridization, the stereoactive lone pair states are also amenable to mixing with Cl 3*p* states. These results have been further corroborated by first-principles DFT calculations and XANES spectra.[34] Similarly, in $FeSb_2O_4$, F-ion insertion and coordination of F-ions to Sb^{3+} centers destabilizes Sb—O interactions and shifts them higher in energy (Fig. 2g).[40] Oxyhalides of Pb and Bi have been shown to possess appropriately positioned valence bands for photocatalytic evolution of hydrogen.[79] Dual control over the design space (choice of p-block cation and anion) would allow us to synthesize a library of p-block oxyhalides with two independently tunable variables to optimize valence band energy positioning for hole transfer with QDs, enabling ultrafast and more effective excited-state charge separation and yielding heterostructures for efficient delivery of holes to water oxidation catalysts at a low overpotential. Therefore, the anionic substitution of oxygen provides an important additional vector to Fermi engineer the valence band of compounds containing stereochemically active lone pairs, enables new structural motifs where lone-pair repulsions between cation $5s^2$/$6s^2$ lone pairs and halide lone pairs allow for lattice anharmonicity, and provide a means of improving their band alignment with QDs to achieve faster hole extraction, within heterostructures, by increasing energy dispersion for optimal harvesting of solar energy.

4. Synthesis and Characterization of $M_xV_2O_5$/QD Heterostructures and Determination of Energetic Offsets

Given the diversity and modularity of lone-pair vanadium bronzes and their tunability of mid-gap states, they can be effectively interfaced to extract holes from a diverse range of QDs with varying positions of valence band edges. The QDs are used as harvesters of light and donors of excited charge carriers within the photocatalytic architectures.[22,82] II-VI QDs and related compounds have been deposited onto substrates, and interfaced with other materials components to yield heterostructures, primarily via four methods: (1) chemical bath deposition (CBD), wherein the substrate is immersed in solvated ionic precursors;[83,84] (2) direct attachment, which involves depositing pre-synthesized nanoparticles onto substrates, or interfacing as-synthesized nanoscopic components to yield heterostructures, without the aid of a molecular linker;[85] (3) successive ionic layer adsorption and reaction (SILAR), a variation of CBD in which the substrate is sequentially immersed in different precursor solutions and the metal chalcogenide or related material of interest is precipitated directly onto the substrate;[86,87] and (4) linker-assisted assembly (LAA), in which bifunctional linker molecules tether materials components together to yield heterostructures or nanoparticle-functionalized substrates.[88]

In recent work, we have synthesized $M_xV_2O_5$/QD heterostructures of varying compositions through both SILAR and LAA as illustrated in **Figure 5**.[20,25,29,30] These techniques each have distinct advantages and disadvantages. SILAR yields direct $M_xV_2O_5$/QD interfaces and controllable loadings of QDs encompassing almost complete core/shell geometries, but affords relatively less control over the size and size distribution of deposited QDs. Alternatively, LAA, in which pre-synthesized colloidal QDs are tethered to $M_xV_2O_5$ nanowires via ligands, enables greater control over the size and electronic properties of QDs, and therefore the interfacial energetic offsets that determine the driving force for charge transfer within heterostructures; however, LAA typically yields lower loadings of QDs on $M_xV_2O_5$, and ligands may present a barrier to interfacial charge transfer requiring specific channels such as level crossing of the excited carrier state in QDs with receiving states or superexchange processes to mediate change transfer in donor—bridge—acceptor systems.[89]

In the SILAR deposition of CdSe onto β-$Pb_{0.33}V_2O_5$ nanowires, as an example, the nanowires are initially dispersed in a solution of Cd^{2+}, collected by centrifugation, and washed, and then dispersed in a solution of Se^{2-}, collected, and washed (**Fig. 5A**).[25] This sequence of steps represents one SILAR cycle. The loading and average size of QDs increase with the number of sequential SILAR-deposition cycles, the concentration of precursor solutions, and the reaction time per SILAR cycle.[20,90] SILAR-deposited CdS and CdSe exhibit blue-shifted absorption onsets relative to the bulk materials and are thus in the quantum confinement regime. Approximately 3—10 SILAR cycles are used to deposit II—VI QDs onto $M_xV_2O_5$ or $M_xM'_yV_2O_5$ NWs.

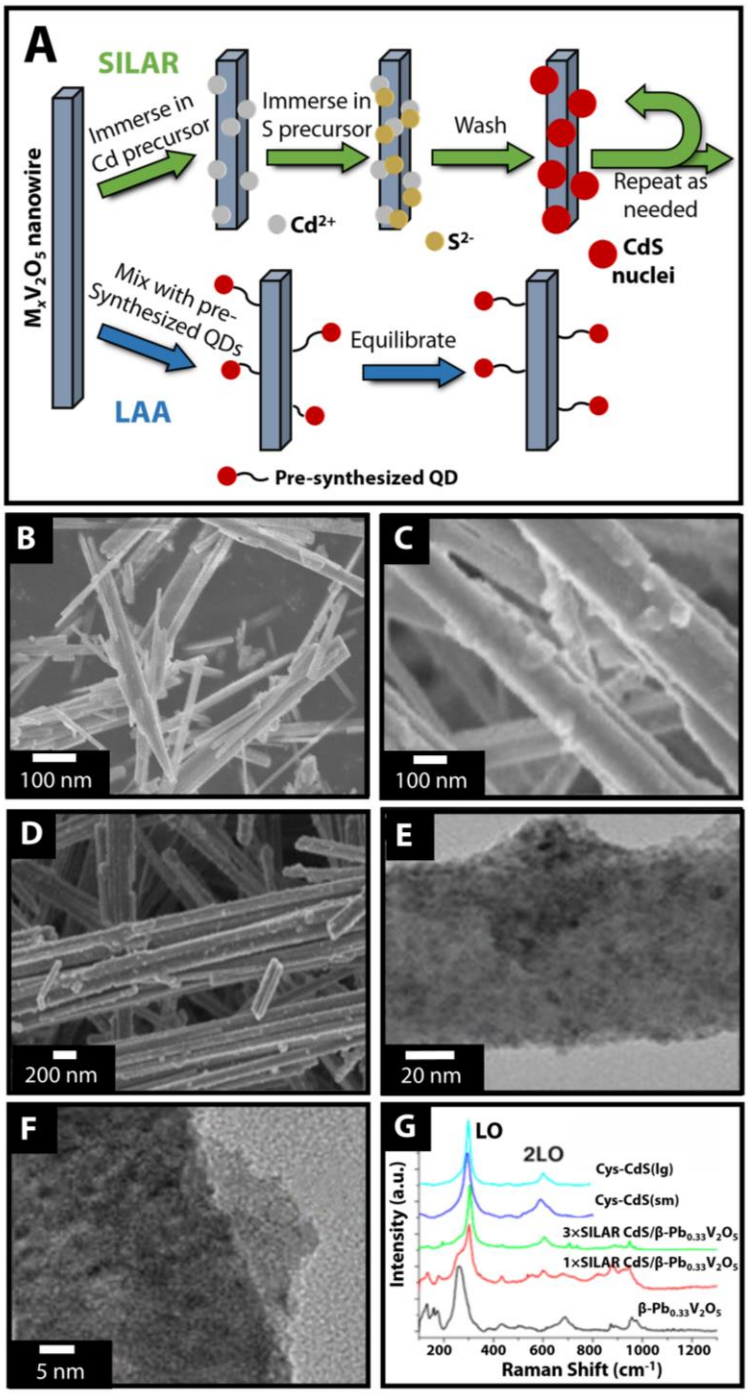

Figure 5. Heterostructures of $M_xV_2O_5$ nanowires and CdS/CdSe quantum dots made by SILAR and LAA. (A) Schematic sketching heterostructure synthesis via SILAR (top) and LAA (bottom) methods. SEM images of **(B)** bare β-$Pb_{0.33}V_2O_5$ NWs, **(C)** LAA-derived cys-CdSe/β-$Pb_{0.33}V_2O_5$ heterostructures, and **(D)** CdSe/β-$Pb_{0.33}V_2O_5$ prepared by 3 SILAR cycles. TEM images of **(E)** CdS/β-$Pb_{0.33}V_2O_5$ after 3 SILAR cycles and **(F)** LAA-derived cys-CdS/β-$Pb_{0.33}V_2O_5$. **(G)** Raman spectra of β-$Pb_{0.33}V_2O_5$, SILAR-derived CdS/β-$Pb_{0.33}V_2O_5$ after 1 or 3 SILAR cycles, and dispersed cys-CdS QDs. Panels **(C)** and **(D)** are adapted with permission from reference (25). Copyright 2015 American Chemical Society. Panels **(E)**, **(F)**, and **(G)** are adapted with permission from reference **(20)**. Copyright 2016 American Chemical Society.

LAA-derived heterostructures are readily prepared by reacting $M_xV_2O_5$ NWs with cysteinate-capped CdSe or CdS QDs (cys-CdSe or cys-CdS) in aqueous dispersions. As-synthesized colloidal CdSe and CdS QDs bearing native cysteine capping groups are particularly suitable for interfacing with $M_xV_2O_5$; the protonated amine of cysteine, under sufficiently acidic conditions, may promote the attachment of the QDs to the NW substrate.[25]

In scanning electron microscopy (SEM) and transmission electron microscopy (TEM) images, $M_xV_2O_5$/CdSe and $M_xV_2O_5$/CdS heterostructures synthesized by either SILAR or LAA exhibit rougher and speckled surfaces (Figs. 5B,C), relative to the bare NWs (Fig. 5A). Well-resolved overlayers of cadmium chalcogenide obscure the lattice planes of the $M_xV_2O_5$ substrate, and discrete QDs are resolvable in high-resolution TEM images.[25] Much recent effort has focused on automated image analysis using machine learning methods.[91] Increasing the number of SILAR cycles leads to agglomeration of the QDs.[20,21,25] The functionalization of QDs on $M_xV_2O_5$ NWs can be verified and quantified by EDS from the presence of Cd and either S or Se within the heterostructures. EDS elemental mapping reveals homogeneous surface coverage of SILAR-deposited CdSe on β-$Sn_{0.23}V_2O_5$ NWs with spatially-resolved domains of CdSe and β-$Sn_{0.23}V_2O_5$.[21] SAED patterns of SILAR- or LAA-derived CdS/β-$Pb_{0.33}V_2O_5$ heterostructures and SILAR CdSe/β-$Sn_{0.23}V_2O_5$ heterostructures are complex, exhibiting diffraction spots for the NWs as well as diffuse ring patterns due to the corresponding QDs. High-resolution TEM images reveal wurtzite lattice fringes for CdS or CdSe QDs in both SILAR- and LAA-derived heterostructures (Fig. 5E,F). The crystal structures of LAA- and SILAR-deposited cadmium chalcogenides on $M_xV_2O_5$ NWs can further be confirmed by Raman spectroscopy (Fig. 5G), through the growth of the bulk longitudinal optic (LO) mode and second-order overtone bands corresponding to CdS or CdSe.[20,25] The energy positioning of midgap states in $M_xV_2O_5$ or $M_xM'_yV_2O_5$ compounds and their alignment with VB edges of QDs, which determines the thermodynamics of hole transfer, can be examined using HAXPES. HAXPES is a non-destructive method to analyze the electronic structure of materials. Given its enhanced probing depth relative to soft X-rays, HAXPES can measure electronic states deep into the bulk (Figure 6A). The photoionization cross-sections of different states measured by HAXPES are rapidly diminished with increasing incident photon energy but their dependences vary strongly as a function of the angular momentum quantum number of the orbitals contributing to the states.[41] The cross-sections of subshells with higher orbital angular momentum quantum numbers, for instance, *f* and *d* subshells, are rapidly diminished as compared to *s* and *p* orbitals.[35,43] As such, HAXPES spectra acquired at higher incident photon energies more prominently feature contributions from subshells with lower angular momentum. Stereoactive lone pair states, which are derived from $5/6s^2$ orbitals of post-transition-metal cations are thus prominently observed at higher incident photon energies.[6,92] HAXPES measurements performed across our available foundry of single crystal samples in conjunction with first-principles simulations and COHP analysis (Fig. 2) thus provide a direct means of evaluating both the energy positioning and dispersion of mid-gap states as well as ascertaining their specific orbital contributions. Figure 6 compares HAXPES spectra acquired for β-$Pb_xV_2O_5$ and β-$Sn_xV_2O_5$ (**Fig. 6B**) and β-$Sn_xV_2O_5$ with and without CdSe/CdTe QDs deposited by SILAR (**Fig. 6C**). The HAXPES data demonstrate the modulation of the mid-gap state by replacing Pb^{2+} with Sn^{2+}, which enables improved overlap with the valence band edges of CdSe and CdTe QDs. Figure 6D sketches the energetic offsets as derived from HAXPES and DFT

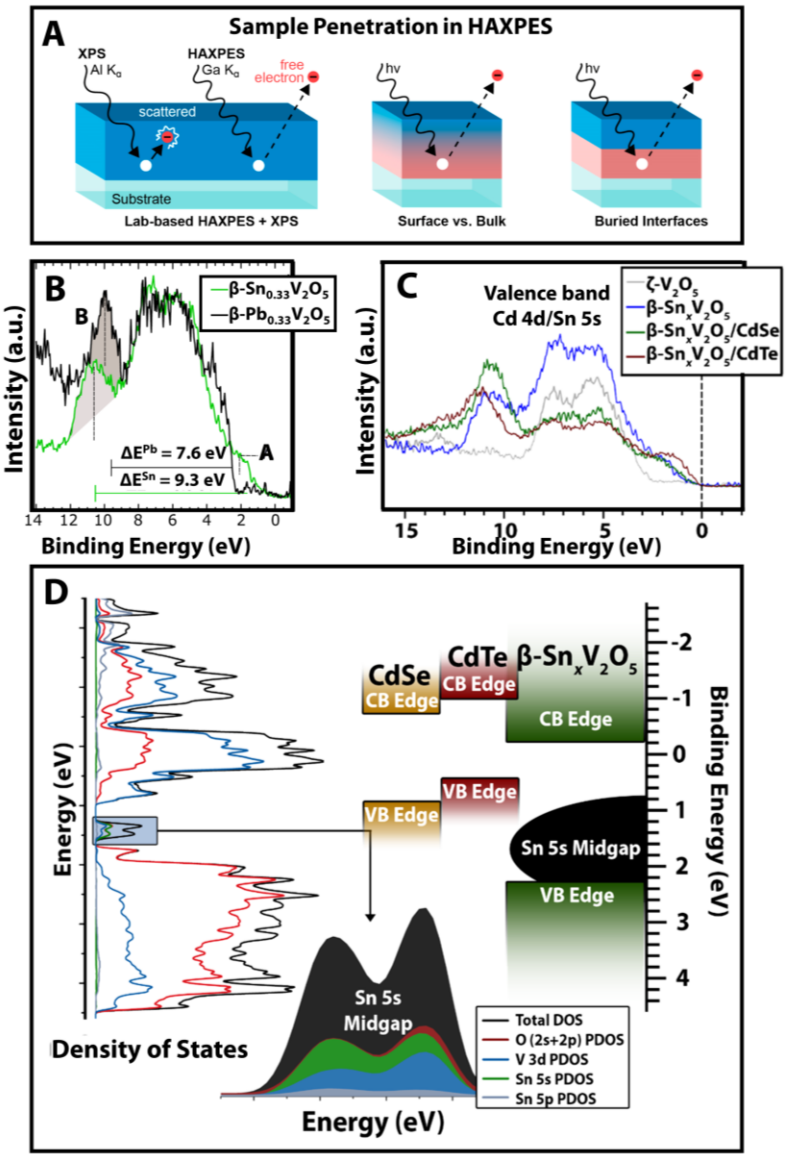

Figure 6. HAXPES as a tool for probing energetic contributions. (A) Diagram illustrating the capacity for HAXPES to probe bulk sample as well as buried interfaces, compared to conventional XPS. **(B)** HAXPES spectra comparing β-$Sn_{0.33}V_2O_5$ and β-$Pb_{0.33}V_2O_5$ nanowires illustrating the difference in energy positioning across lone-pair bronzes as well as the change in distribution of bonding and antibonding states (labeled B and A, respectively). **(C)** HAXPES spectra comparing empty ζ-V_2O_5 nanowires, bare β-$Sn_{0.33}V_2O_5$, and β-$Sn_{0.33}V_2O_5$ interfaced with CdSe and CdTe QDs. **(D)** Illustration of energetic offsets arising from CdSe, CdTe, and $M_xV_2O_5$ interfaces, and consequent density of states (left-hand side) and HAXPES-measurable binding energies (right-hand side), that can be modulated by choice of lone-pair cation. Panels **(A)** and **(B)** are adapted from reference (6). Licensed under CC BY 4.0 / reformatted and relabeled from original. Panels **(C)** and **(D)** are reproduced with permission from reference (21). Copyright 2018 American Chemical Society.

calculations illustrating the thermodynamic favorability of QD-to-mid-gap-state hole transfer. The CB edges of QDs are established using diffuse reflectance spectroscopy and X-ray absorption

spectroscopy. These measurements together enable mapping of the thermodynamic driving forces for charge separation and the potentials (versus SHE) at which photogenerated electrons and holes are expected to be delivered to co-catalysts. Energetic offsets and thermodynamic driving forces can be derived across the extensive design space of $M_xV_2O_5$ or $M_xM'_yV_2O_5$ and interfaced II-VI and III-V QDs by interrogating libraries with HAXPES and diffuse reflectance spectroscopy measurements. By revealing which heterostructures have energetic offsets that promote the desired QD-to-mid-gap-state hole transfer underpinning photocatalysis, and by enabling understanding of the influence of electronic structure on charge-transfer dynamics, HAXPES further serves as the linchpin of an accelerated exploration strategy.

5. Ultrafast Interfacial Charge Separation by Design

Optimal thermodynamic alignments as illustrated in Figure 1B are necessary but not sufficient for effective charge separation within photocatalytic heterostructures; effective charge separation also requires ultrafast electron and hole transfer to prevent recombination and unproductive channels that do not yield photoproducts. Excited electrons and holes must be separated efficiently in photocatalysis, such that desired reduction and oxidation reactions (Figure 7A, A-F) outcompete electron-hole recombination (Figure 7A, 1-5).[14,15] For a system with a continuum of donor or acceptor states, charge-transfer rate constants depend on the thermodynamic driving force, reorganization energy, electronic coupling, and the density of charge-accepting states.[93,94] The kinetics and thermodynamics of charge-transfer processes driving photocatalysis are thus

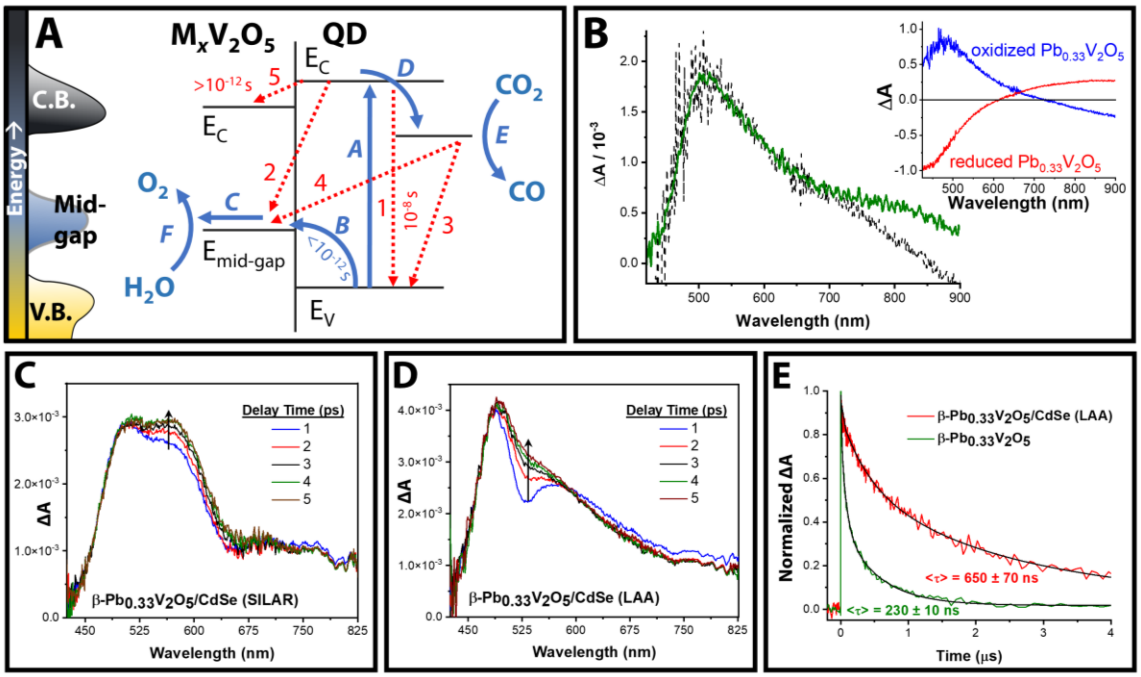

Figure 7. Charge-Transfer Kinetics Underpinning Charge Separation and Photocatalysis. (A) Photoinduced charge-transfer cascade leading to photocatalysis, with reduction of CO_2 to CO as a representative example (arrows A—F), and competing recombination pathways (arrows 1—5), with measured timescales. The left schematic represents the corresponding band structure of $M_xV_2O_5$. **(B)** Measured Transient Absorption (TA) spectrum (green) of β-$Pb_{0.33}V_2O_5$ and fit (black) to linear combination of absorbance spectra (shown in inset) of electrochemically oxidized and reduced β-$Pb_{0.33}V_2O_5$ (the latter have been derived from spectroelectrochemical measurements). **(C, D)** TA spectra acquired at delay times of 1—5 ps for SILAR-derived **(C)** and LAA-derived **(D)** β-$Pb_{0.33}V_2O_5$/CdSe heterostructures; the instantaneous rise of induced absorbance from 475—525 nm reveals sub-picosecond hole transfer whereas the time-resolvable growth of absorbance at longer wavelengths arises from the decay of the first excitonic bleach of CdSe with electron transfer. **(E)** Charge-separated state lifetimes ($<\tau>$), monitored via the decay of induced absorption at 510 nm, are substantially longer for β-$Pb_{0.33}V_2O_5$/CdSe heterostructures as compared to bare β-$Pb_{0.33}V_2O_5$. Panels **(C)** and **(D)** are adapted with permission from reference (19). Copyright 2016 American Chemical Society.

intertwined. We have measured sub-picosecond transfer of holes from valence band edges of QDs to midgap states of $M_xV_2O_5$ in our CdS/β-$Pb_{0.33}V_2O_5$, CdSe/β-$Pb_{0.33}V_2O_5$ and CdSe/β-$Sn_{0.23}V_2O_5$ heterostructures, and have discovered that charge-transfer mechanisms and dynamics depend on composition, electronic structure, energetic offsets, and interconnectivity.[19–22,30] Key interfaces include between (i) QDs and $M_xM'_yV_2O_5$ NWs which require hole-transfer channels (as sketched in Figure 1) and (ii) QDs and co-catalysts (such as Pt or MoS_2) which necessitate electron-transfer channels.

Hole-transfer dynamics and yields as a function of interfacial electronic structure and energetic offsets driving hole transfer have been found to be governed by (1) properties of mid-gap states of NWs, (2) size and composition of QDs (tunable by doping and alloying), and (3) QD/NW connectivity and interfacial electronic coupling. Emission-quenching experiments in concert with transient absorbance (TA) spectroscopy have revealed charge-transfer mechanisms, dynamics, and yields in our heterostructures as a function of these parameters and have been interpreted with the help of spectroelectrochemical measurements (Fig. 7B). Transfer of holes to mid-gap states of $M_xV_2O_5$ and $M_xM'_yV_2O_5$ can be quantified via an induced absorption (475—525 nm);[19,20] sub-picoscond hole transfer is observed from photoexcited CdSe and CdS QDs to $M_xV_2O_5$, whereas in binary heterostructures and in the absence of a reduction co-catalyst, QD-to-$M_xV_2O_5$ electron transfer proceeds on 4—5 ps timescales for SILAR heterostructures and more slowly still for LAA heterostructures (Fig. 7C). Differential rates of electron and hole transfer effect charge separation, and electron-hole recombination is substantially slower for heterostructures than for bare $M_xV_2O_5$ (Fig. 7D). Addition of a co-catalyst capable of electron extraction from photoexcited QDs further enhances charge separation in ternary photocatalytic architectures used as the active elements of photoelectrochemical cells. Spectroelectrochemical and TA measurements on free QDs and NWs, and QD/V_2O_5 heterostructures (without mid-gap states), enable us to assign features to charge transfer.[19,29] The availability of a library of $M_xV_2O_5$ or $M_xM'_yV_2O_5$ and interfaced II-VI and III-V QDs provides opportunities for measuring the kinetics of excited-state interfacial hole transfer for novel heterostructures building on detailed understanding of thermodynamic energetic offsets.

6. Photocatalysis

The light-harvesting properties and ultrafast charge separation, via excited-state hole transfer, exhibited by various $M_xV_2O_5$/QD heterostructures renders these materials intriguing candidates for applications in photocatalysis.[21] Much of the experimental demonstrations of photocatalysis on these systems pertains to HER, or the reduction half-reaction of water splitting, with our $M_xV_2O_5$/QD heterostructures.[30] We have characterized photocatalytic HER using photoelectrochemistry (PEC). In a typical experiment to evaluate the catalytic function of QD/NW heterostructures, the heterostructures are dispersed in ethanol and spray coated onto a conductive substrate such as fluorine-doped tin oxide (FTO); the heterostructured thin film serves as the working electrode for PEC measurements. A coiled Pt wire and saturated calomel electrode (SCE) are used as the counter and reference electrodes, respectively. A typical electrolyte is KNO_3, lactic acid, and a Ni(3-mercaptopropionic acid) co-catalyst in a 1:4 (*v:v*) water:acetonitrile solution. For H_2 generation experiments, the electrochemical cell is purged with Ar (1 h) and then illuminated (1 h) with a 100 W Xe arc lamp filtered to transmit 400—720 nm light. Following illumination, the headspace is analyzed for the presence of H_2 using gas chromatography (GC).[21,29] In one

approach, linear sweep voltammograms are acquired under chopped white-light illumination of bare $M_xV_2O_5$ (Fig. 8A) and $M_xV_2O_5$/QD heterostructure-functionalized photocathodes (Fig. 8B) to provide direct evidence for light-initiated redox photocatalysis. Additionally, chronocoulometry data are acquired under steady-state white-light illumination, at applied potentials at which dark current is negligible. H_2 is collected and characterized by gas chromatography (GC), and Faradaic efficiencies are calculated from the charge passed and the amount of H_2 evolved.

The combination of these PEC approaches enables straightforward comparisons of the relative rates and efficiencies of HER among various $M_xV_2O_5$/QD heterostructure formulations (Fig. 8C). We have also characterized photocatalytic HER from dispersed $M_xV_2O_5$/QD heterostructures under white-light illumination, where H_2 is collected and characterized by GC; thus, the heterostructures can promote HER within dispersions and without any applied bias. In both approaches, PEC and photocatalysis with dispersed heterostructures, we have oxidized lactic acid rather than water, such that the oxidation half reaction does not limit the rate of HER, and we use solvated nickel(II) co-catalysts to enhance the rate of HER from $M_xV_2O_5$/QD heterostructures.

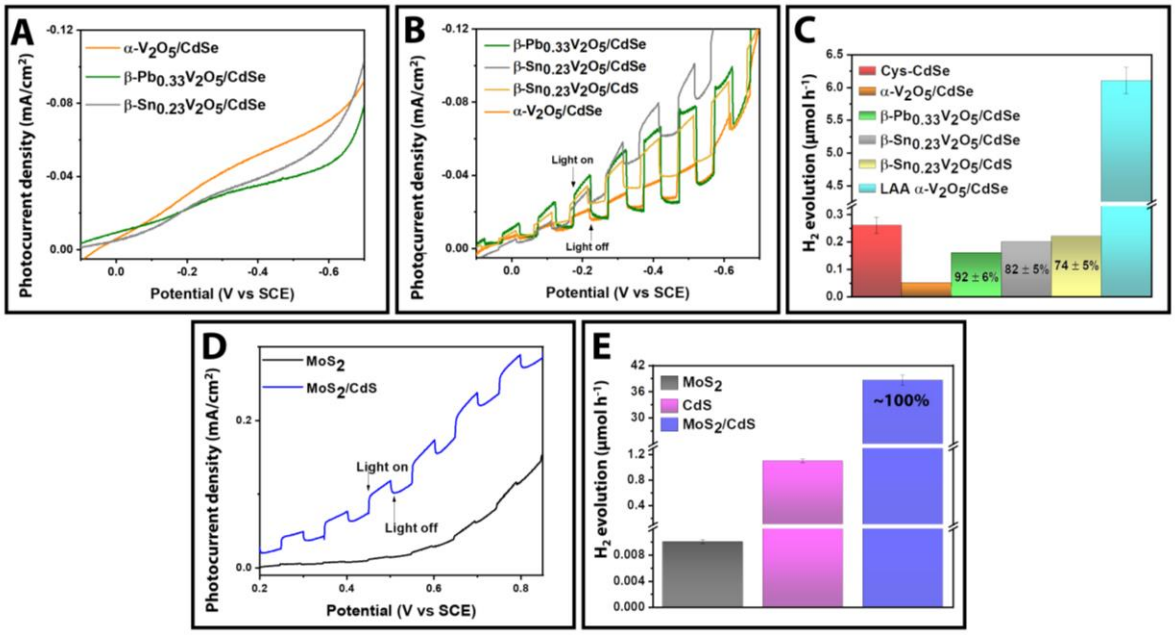

Figure 8. Photocatalytic reactivity of $M_xV_2O_5$/QD heterostructures. (A) Linear sweep voltammograms of bare α-V_2O_5 (orange), β-$Pb_{0.33}V_2O_5$ (green), and β-$Sn_{0.23}V_2O_5$/CdS (grey) NWs under chopped illumination exhibiting negligible photocurrents and **(B)** linear sweep voltammograms of the corresponding $M_xV_2O_5$/QD heterostructures. **(C)** Rates of H_2 evolution for SILAR-derived heterostructures (PEC) and LAA-derived α-V_2O_5/CdSe heterostructures (PC) with respective Faradaic efficiencies indicated. **(D)** Linear sweep voltammograms of bare MoS_2 (black) and MoS_2/CdS heterostructures (blue) and **(E)** corresponding rates of H_2 evolution for bare MoS_2, isolated CdS QDs, and MoS_2/CdS heterostructures with measured Faradaic efficiency indicated. Panel **(D)** is adapted with permission from reference (30). Copyright 2020 American Chemical Society.

In our initial characterization of photocatalytic HER, β-$Pb_{0.33}V_2O_5$/CdSe heterostructures exhibited a 3-fold enhancement in reductive photocurrent relative to α-V_2O_5/CdSe heterostructures (Fig. 8a).[22] Whereas α-V_2O_5 lacks mid-gap states, this result illustrated that excited-state hole transfer from CdSe to mid-gap states of β-$Pb_{0.33}V_2O_5$ could indeed facilitate extended charge separation and redox photocatalysis. Both SILAR- and LAA-derived β-$Pb_{0.33}V_2O_5$/CdSe heterostructures evolved H_2 with Faradaic efficiencies exceeding 90% (Fig. 8B), indicating that HER was the predominant electrochemical mechanism.[22] Our second-generation β-$Sn_{0.23}V_2O_5$/QD heterostructures also exhibited reductive photocurrents and HER (Fig. 8A), with Faradaic efficiency of 82±5% for β-$Sn_{0.23}V_2O_5$/CdSe. No photocurrent was observed for bare β-$Sn_{0.23}V_2O_5$ electrodes, again highlighting the role of mid-gap states and interfacial charge separation in HER. At an applied potential of (-0.171 ± 0.007) V versus SCE, the photocurrent observed for β-$Sn_{0.23}V_2O_5$/CdSe was within 50% of the photocurrent produced by β-$Pb_{0.33}V_2O_5$/CdSe; the respective Faradaic efficiencies were comparable, and the H_2 evolution rates were within ca. 20% of one another. Notably, despite differences in measured reductive photocurrents in LSV measurements, which indicate the rate and yield of reduction processes irrespective of mechanism, the measured Faradaic efficiencies were high (above 80%) for all $M_xV_2O_5$/QD heterostructures (Fig. 8B). Thus, irrespective of composition, HER is the predominant photocatalytic reduction mechanism for $M_xV_2O_5$/QD heterostructures.

We have further characterized HER from α-V_2O_5/CdSe heterostructures in some detail. These heterostructures have type-II interfaces that drive electron transfer from photoexcited CdSe to the conduction band of α-V_2O_5.[29] The charge-separation mechanism at the α-V_2O_5/CdSe interface, QD-to-NW electron transfer, is thus the reverse of the mechanism for $M_xV_2O_5$/QD heterostructures. Under prolonged illumination of dispersions, HER from LAA-derived α-V_2O_5/CdSe was 20-fold more efficient relative to colloidal cys-CdSe QDs, illustrating that interfacial charge separation indeed promotes redox photocatalysis. Properties of the α-V_2O_5/CdSe interface greatly affect HER. SILAR-derived α-V_2O_5/CdSe heterostructures evolved H_2 at a rate of <0.05 μmol h^{-1}, whereas corresponding LAA-derived heterostructures evolved H_2 100-fold more rapidly at 6.1 ± 0.2 μmol h^{-1}. We attributed the slower HER at SILAR-derived α-V_2O_5/CdSe heterostructures to rapid electron-hole recombination at interfaces with direct contact between CdSe and α-V_2O_5, whereas, for LAA-derived heterostructures, the presence of cysteine as a molecular linker further separates electrons and holes and provides a barrier to recombination.[29]

In an effort to eliminate the need for solvated co-catalyst, and towards the goal of preparing ternary heterostructure photocatalysts, we have recently synthesized MoS_2/CdS heterostructures, via SILAR deposition of CdS onto MoS_2 nanoplatelets, and characterized their electronic structure, excited-state charge transfer reactivity, and photocatalytic performance.[30] MoS_2/CdS heterostructures exhibited Type-II energetic offsets, with band-edge potentials of CdS lying negative relative to those of MoS_2. Photoexcited electrons in CdS QDs were transferred within 5 ps to MoS_2, thus separating photogenerated charges to facilitate redox photocatalysis. Time-dependent DFT simulations indicate that level crossing and orbital mixing of excited states facilitated by the charge-separation dipole underpins ultrafast electron transfer in CdS/MoS_2 heterostructures. Resonantly matched states, identifiable from TDDFT-MD and tunable with crystal facet and composition (e.g., Cd-terminated CdS(001)/MoS_2) are a key descriptor for

ultrafast electron transfer underpinning effective charge separation and photocatalytic function.[89] The MoS_2/CdS heterostructures evolved H_2 at a rate of 38.6 ± 1.2 μmol h^{-1} with Faradaic efficiency approaching 100% (Fig. 8E). In contrast, electrodes functionalized with bare MoS_2 nanoplatelets did not produce any appreciable photocurrent (Fig. 8D). These results illustrate the scope for exploring SILAR- and LAA-derived MoS_2/QD heterostructures of varying compositions and electronic structure, as well as ternary heterostructures incorporating MoS_2, QDs, and $M_xV_2O_5$ or $M_xM'_yV_2O_5$, towards the goal of eliminating altogether the need for solvated co-catalysts.

7. Prospects for Improved Navigation of the Design Space

The future design of photocatalytic materials requires navigating a design space with an imposing number of process variables: Even when limited to lone-pair vanadium bronzes, as described above, species can be accessed in both stable and metastable regions of multidimensional phase spaces, targeting compounds with the insertion and removal of multiple cations and anions, to be interfaced within binary or even ternary heterostructures, and accessed by a wide array of synthetic strategies. More generally, for any given composition, there are an infinite number of possible metastable configurations, which some believe might even represent a formally nondeterministic polynomial-time (NP) hard problem.[95,96] Even for a polynomial problem, the number of possible combinations increases as a cubic relationship in the number of parameters; as such, it remains almost entirely beyond the scope of full factorial experiments. For $O(N^3)$ order, with 10 parameters, there are 1,000 combinations to explore; addition of 100 parameters implies 1 million combinations. As such, the improved navigation of this many-dimensional design space requires the judicious use of informatics and machine learning capable of processing large volumes of chemical information and of AI reaction discovery with integration of physical design principles.

The degree to which a set of atoms is able to prospect its available energy landscape depends in substantial measure on (i) the starting energy with which the material begins its relaxation towards a (meta)stable equilibrium state; (ii) available reaction trajectories (governed by the functional that describes the landscape, the entry points where monomers enter this landscape, and the specifics of precursor structure); and (iii) accessibility of transformation paths between adjacent metastable states (reflecting the propensity for the material to be trapped within a shallow valley).[17,97] Since computational simulations of multidimensional free energy landscapes remain intractable, AI models hold promise as surrogates to aid the navigation of high-dimensional spaces.

For targeting mid-gap states in lone-pair vanadium bronzes, the relevant chemical descriptors weighing on the outcome can largely be broken down into structural polymorph, framework connectivity, cation(s), and anion as outlined in in Figure 3; and as we have established, a large diversity of ternary and quaternary structures can be accessed as multidimensional data points. High-throughput synthesis by computerized SILAR apparatuses and ChemSpeed robotic arm platforms allow for the relatively rapid generation of structural information and adjustment of design space parameters. Recently, graph neural networks (GNNs) have been intensively studied to automatically learn features from input graphs for property prediction. The most widely-used architectures for GNNs are message passing neural networks (MPNNs), which update node

features through passing messages across nodes and edges.[17,98] However, GNNs oftentimes fail to consider the important 3D positional information of the original objects. Such 3D information is of pivotal importance to predicting crystal structure outcomes, such as bond lengths, polyhedral distortions, and long-range bonding motifs. 3D graph neural networks (3D GNNs), that explicitly encode 3D positional information about molecular and materials composition and structure, or GNNs capable of learning low-dimensional embedding manifold in a high-dimensional design space,[99] will enable reaction precursors to be mapped to intermediates and final products—thereby establishing proxies for the most probable reaction trajectories.

The mathematical behavior of traditional material precursor—crystal-structure—property functions is inadequate to model far-from equilibrium materials. Instead, optimal recovery models based on evaluating the functional dependence of a rich class of functions (Gaussian Process, Trees, Deep Neural Networks, etc.) are needed to enable identification of design parameters *x* (input features) for which f (*x*) is optimal (proper control of the input features which will optimize the desired material output—a specific crystal structure or energy positioning of states). Materials discovery frameworks that enable the dynamic building and exploitation of internal representations

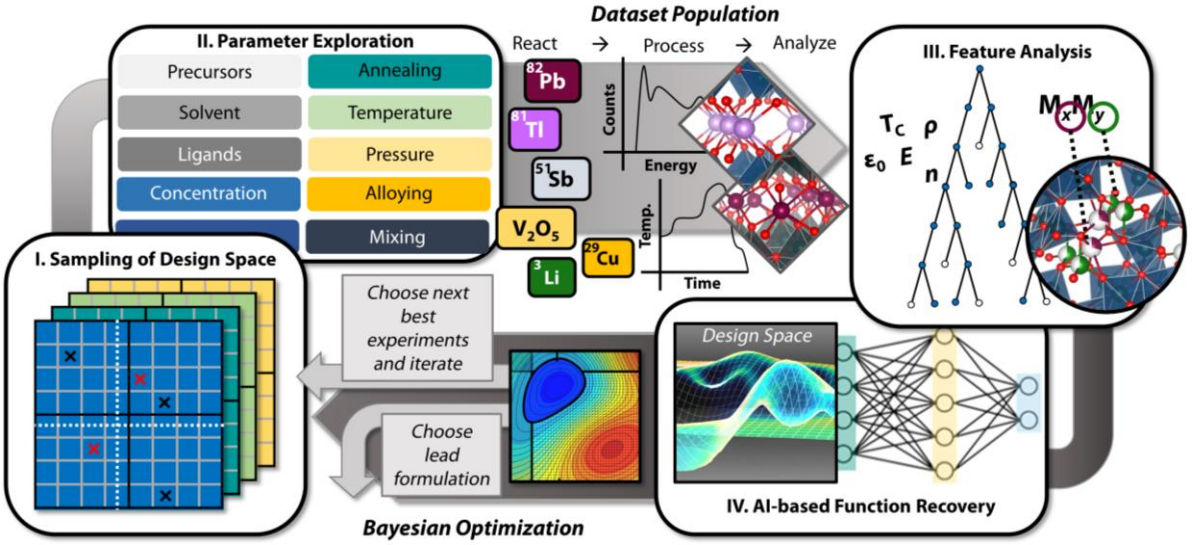

Figure 9. Schematic depiction of a machine-learning workflow for the iterative exploration and exploitation of synthetic design space for identifying active variables that determine structural motifs and crystal structure outcomes in a range of metastable $M_xV_2O_5$ and $M_xM'_yV_2O_5$ polymorphs.

of the materials space, under extreme data sparsity, are required to enable identification of specific modifications (dopant incorporation, structural modification, stress, interfacial properties, external excitation) that will allow for stabilization of metastable polymorphs.

Ternary and quaternary vanadium bronzes, given the plethora of known and accessible structures, provide an excellent platform for algorithmically mapping (Precursor Structure)—(Crystal Structure Outcome)—(Energy Positioning of Mid-Gap States) relationships to connect initial compositions and structures of precursors to crystal structure outcomes, and to the response surface through potentially complex process paths determined by reaction conditions and

iteratively modified using robotic synthesis tools. A learning approach that connects points on a response surface and yields generalizable chemical design principles for metastable materials can be used not only to explore/exploit the available design space but also to augment it. **Figure 9** depicts a schematic of a machine-learning workflow for developing such an iterative approach.

8. Prospects for Photocatalysis Beyond Hydrogen Evolution

Key properties of $M_xV_2O_5$/QD and $M_xM'_yV_2O_5$/QD heterostructures render them ideal for photocatalysis, potentially across a broad spectrum of reactions initiated by reduction or oxidation events: (1) absorption spectra are tunable with the size, composition, and surface functionalization of QDs and the composition of $M_xV_2O_5$ or $M_xM'_yV_2O_5$; (2) interfacial electronic structure is programmable with composition and interconnectivity, which in turn enables control of the driving force for charge transfer and the overlap between donor and acceptor states (as illustrated in **Figures 1** and **3**); (3) the ultrafast extraction of holes from QDs[19,20] prevents photoanodic corrosion (**Fig. 7**); and (4) QDs can be interfaced with reduction co-catalysts such as MoS_2. In past work, we have described several generations of heterostructures with systematically improved interfacial energetics to drive photoinduced hole transfer.[19–21] Charge separation can be exploited in photocatalytic HER with high Faradaic efficiencies.[21,22] Section 3 describes a substantially expanded foundry of new $M_xM'_yV_2O_5$ materials with diverse compositions and atomistic and electronic structures, which promises to enable still greater control over interfacial charge transfer and charge transport. These new materials and heterostructures further hold promise for broadening the scope of redox reactions catalyzed by photoexcited $M_xV_2O_5$/QD and $M_xM'_yV_2O_5$/QD heterostructures.

Several important redox reactions, for which photocatalysts are highly sought-after, share similar mechanisms and have common thermodynamic and kinetic requirements, and are thus ripe for exploration with a tunable photocatalyst platform.[21,22,30] Oxidizing water rather than a sacrificial donor, and thus splitting water into hydrogen and oxygen, could provide a sustainable route to hydrogen as a carbon-neutral fuel. To split water with our heterostructures will require interfacing new or established water-oxidation catalysts either with dark anodes of photoelectrochemical cells or directly with $M_xV_2O_5$ or $M_xM'_yV_2O_5$ in dispersed photocatalysts.

The $M_xV_2O_5$/QD and $M_xM'_yV_2O_5$/QD heterostructure platform may also be applicable towards the photocatalytic reduction of CO_2, which is particularly challenging because HER competes with the reduction of CO_2, and because of the broad distribution of potential CO_2-reduction products. Thermalized electrons at E_C of many bulk and quantum-confined II-VI and III-V semiconductors lie at potentials sufficiently negative to reduce CO_2 to C1 products (**Fig. 1B**). Photocatalytic reduction of both CO_2 and H^+ are thus thermodynamically favorable. To promote the selective reduction of CO_2 may require doping the QDs[100] or interfacing QDs with CO_2-reduction co-catalysts, potentially including MoS_2 or other transition metal chalcogenides.[101–109] Recent reports have highlighted the potential to control products of photocatalytic reduction of CO_2 or H^+ with the size of QDs.[110,111] Products of CO_2 reduction at $M_xV_2O_5$/QD and $M_xM'_yV_2O_5$/QD heterostructures may thus depend on the energy of electrons in QDs. A range of

II-VI and III-V QDs, readily interfaced with $M_xV_2O_5$ or $M_xM'_yV_2O_5$ surfaces via SILAR or LAA, have bulk E_c values within and more negative than relevant CO_2-reduction potentials (**Fig. 1B**). For example, the E_c of bulk CdSe is more negative than the CO_2/CH_4 couple and more positive than the CO_2/CO couple, whereas, with decreasing size of CdSe QDs, the reduction of CO_2 to CO will become thermodynamically favorable. The influence of both thermodynamics and kinetics (relative activation barriers for various reduction pathways) on CO_2-reduction product distributions is ripe for exploration with the $M_xV_2O_5$/QD and $M_xM'_yV_2O_5$/QD heterostructure platform.

Finally, heterostructures that produce long-lived charge-separated states with electrons and holes at sufficiently reducing and oxidizing potentials, respectively, can be used to photocatalyze wide-ranging redox processes involving organic transformations or the production of chemical feedstocks. Indeed, various QDs have recently been shown to photocatalyze organic reactions including carbon-carbon bond formation reactions, cycloadditions, and polymerizations.[112–115] Within $M_xV_2O_5$/QD and $M_xM'_yV_2O_5$/QD heterostructures, charge-separated states are long-lived and photoanodic corrosion of QDs is negligible; moreover, the many compositional, structural, electronic, and interfacial degrees of freedom of the heterostructures afford an unusual degree of control over electronic properties, excited-state charge transfer, and photocatalytic reactivity. Thus, this heterostructure platform holds promise for mediating a rich landscape of photocatalysis mechanisms, which the focus of extensive ongoing research.

Author Biographies

Joseph V. Handy is currently a Ph.D. candidate in the Department of Chemistry at Texas A&M University under the advisement of Sarbajit Banerjee. His research focuses on the guided exploration of V_2O_5 phase space in order to precisely modulate electronic and atomistic structure for the design of new materials. Joseph is a Vanitec and Welch Foundation Fellow. He received his B.S. in Chemistry from the College of William & Mary in 2017.
ORCID ID: 0000-0002-0106-9865

Wasif Zaheer obtained his undergraduate degree from the School of Science and Engineering at Lahore University of Management Sciences, Pakistan. He is currently a Ph.D. candidate at Texas A&M University and an Advanced Light Source Doctoral Fellow in residence at Lawrence Berkeley National Laboratory. His research interests are focused on the design and synthesis of new materials, fundamental X-ray spectroscopy characterization, and computational modeling to decipher mechanisms of operation of anion batteries and water-splitting photocatalysts.

Arianna R. M. Rothfuss is a Ph.D. candidate in the Department of Chemistry at the University of Buffalo (UB). Her current work focuses on accomplishing water splitting via interfacing quantum dots with various low dimensional materials.
ORCID ID: 0000-0003-2593-8428

Caitlin R. McGranahan is currently a Ph.D. candidate in the Department of Chemistry at the University at Buffalo under the advisement of Professor David Watson. Her current research focuses on characterization of photoinduced interfacial charge-transfer dynamics within dual-quantum dot (QD) heterostructures, both colloidal and surface-immobilized, and QD-molecular

acceptor heterostructures; working towards applications in photocatalysis and solar energy conversion, as well as characterization of photoelectrochemical hydrogen evolution from QD-nanowire heterostructures.
ORCID ID: 0000-0002-2978-4190

George Agbeworvi obtained his undergraduate degree from Kwame Nkrumah University of Science and Technology (KNUST), Ghana, and his masters degree from North Carolina A&M State University, Greensboro. He also received his Ph.D. from Purdue University, West Lafayette, and is currently a Postdoctoral Associate at Texas A&M University. His research involves the design, synthesis, and characterization of metastable materials for electronic and magnetic properties as well as electrochemical energy storage.

Justin L. Andrews received his Ph.D. from Texas A&M University under the advisement of Sarbajit Banerjee. His research focused on the design of chemical approaches for tuning the electronic properties of metastable solid-state materials. These research efforts have led to applications in energy storage, neuromorphic computing, and photocatalysis. Justin is currently in a postdoctoral research position at the Massachusetts Institute of Technology. Justin received his B.A. in Chemistry from Gordon College.
ORCID ID: 0000-0003-2348-3562

Karoline E. García-Pedraza is a second-year Ph.D. student in Chemistry at the University at Buffalo (UB) under the advisement of David F. Watson. Her research focuses on synthesizing semiconducting inorganic nanomaterials, functionalizing their surface, and exploiting their photocatalytic properties. Karoline is a Schomburg Fellow and holds a BA in Chemistry from the University of Puerto Rico at Cayey.
ORCID ID: 0000-0003-3293-4548

John D. Ponis is a second-year Chemistry graduate student working in the Banerjee Research Group at Texas A&M University. His research targets the synthesis and characterization of novel transition metal oxides with tunable instabilities in electronic and atomic structure. He received his BS in Chemistry from Kutztown University in 2011 and worked in product development for International Chemical Company in Philadelphia before joining Texas A&M in 2019.

Jaime R. Ayala is currently a second-year Chemistry Ph.D. student at Texas A&M University working in the Banerjee group. He obtained his undergraduate degree in chemistry from the University of Texas at El Paso. Jaime is an Innovation in Buildings (IBUILD) Graduate Research Fellow funded by the Department of Energy Building Technologies Office.
ORCID ID: 0000-0003-2730-4525

Yu Ding is the Mike and Sugar Barnes Professor of Industrial & Systems Engineering at Texas A&M University and Associate Director for Research Engagement of Texas A&M Institute of Data Science. Dr. Ding received his Ph.D. degree from the University of Michigan in 2001. His research interest is in data and quality science. Dr. Ding is a Fellow of IISE and ASME and is serving as the Editor-in-Chief for IISE Transactions (2021-2024).

David F. Watson is a Professor and Chair of the Department of Chemistry at the University at Buffalo. His research interests involve designing and synthesizing nanostructured materials, heterostructures, and interfaces for photocatalysis and solar energy conversion, and studying excited-state charge-transfer processes using spectroscopy, photochemistry, and electrochemistry. ORCID ID: 0000-0003-1203-2811

Sarbajit Banerjee is a Davidson Chair Professor of Chemistry, Professor of Materials Science and Engineering, and Chancellor EDGES Fellow at Texas A&M University. His research interests are focused on chemical bonding in metastable solids, electron-correlated compounds, energy conversion and storage, and energy-efficient computation. Recent research recognitions include the Edith and Peter O'Donnell Award in Science, NASA NIAC Fellowship, Beilby Medal, and Rosenhain Medal. He is a Fellow of the Royal Society of Chemistry and the Institute of Physics. ORCID ID: 0000-0002-2028-4675

Acknowledgements

We acknowledge extensive discussions with Louis Piper (Warwick University), Peihong Zhang (University at Buffalo), Bani Mallick (Texas A&M University), and Shengbai Zhang (RPI). The authors acknowledge primary support from the NSF under DMREF-1627197 and DMREF-1626967. We further acknowledge support from NSF Award CMMI-2038625 as part of the NSF/DHS/DOT/NIH/USDA-NIFA Cyber-Physical Systems Program. The research was funded in part by award A-1978-20190330 from the Welch Foundation. W.Z. acknowledges the support from the Advanced Light Source (ALS) doctoral fellowship in residence. The Advanced Light Source is supported by the Director, Office of Science, Office of Basic Energy Sciences, U.S. Department of Energy under contract DE-AC02-05CH11231.

References

(1) Livingston, J. E.; Rummukainen, M. Taking Science by Surprise: The Knowledge Politics of the IPCC Special Report on 1.5 Degrees. *Environ. Sci. Policy* **2020**, *112*, 10–16. https://doi.org/10.1016/J.ENVSCI.2020.05.020.

(2) Millar, R. J.; Fuglestvedt, J. S.; Friedlingstein, P.; Rogelj, J.; Grubb, M. J.; Matthews, H. D.; Skeie, R. B.; Forster, P. M.; Frame, D. J.; Allen, M. R. Emission Budgets and Pathways Consistent with Limiting Warming to 1.5 °C. *Nat. Geosci. 2017 1010* **2017**, *10* (10), 741–747. https://doi.org/10.1038/ngeo3031.

(3) Allen, M.; Dube, O. P.; Solecki, W.; Aragón-Durand, F.; Cramer, W.; Humphreys, S.; Kainuma, M.; Kala, J.; Mahowald, N.; Mulugetta, Y. *Global Warming of 1.5° C. An IPCC Special Report on the Impacts of Global Warming of 1.5° C above Pre-Industrial Levels and Related Global Greenhouse Gas Emission Pathways, in the Context of Strengthening the Global Response to the Threat of Climate Change, Sustainable Development, and Efforts to Eradicate Poverty*; IPCC, 2018.

(4) Sun, Z.; Ma, T.; Tao, H.; Fan, Q.; Han, B. Fundamentals and Challenges of Electrochemical CO2 Reduction Using Two-Dimensional Materials. *Chem* **2017**, *3* (4),

560–587. https://doi.org/10.1016/J.CHEMPR.2017.09.009.

(5) Rosenthal, J. Progress toward the Electrocatalytic Production of Liquid Fuels from Carbon Dioxide. *Prog Inorg Chem* **2014**, *59*, 299–338.

(6) Razek, S. A.; Popeil, M. R.; Wangoh, L.; Rana, J.; Suwandaratne, N.; Andrews, J. L.; Watson, D. F.; Banerjee, S.; Piper, L. F. J. Designing Catalysts for Water Splitting Based on Electronic Structure Considerations. *Electron. Struct.* **2020**, *2* (2), 023001. https://doi.org/10.1088/2516-1075/AB7D86.

(7) He, J.; Janáky, C. Recent Advances in Solar-Driven Carbon Dioxide Conversion: Expectations versus Reality. *ACS Energy Lett.* **2020**, *5* (6), 1996–2014. https://doi.org/10.1021/ACSENERGYLETT.0C00645.

(8) Costentin, C.; Drouet, S.; Robert, M.; Savéant, J.-M. A Local Proton Source Enhances CO2 Electroreduction to CO by a Molecular Fe Catalyst. *Science (80-.).* **2012**, *338* (6103), 90–94. https://doi.org/10.1126/SCIENCE.1224581.

(9) Kothandaraman, J.; Goeppert, A.; Czaun, M.; Olah, G. A.; Prakash, G. K. S. Conversion of CO2 from Air into Methanol Using a Polyamine and a Homogeneous Ruthenium Catalyst. *J. Am. Chem. Soc.* **2016**, *138* (3), 778–781. https://doi.org/10.1021/JACS.5B12354.

(10) Alain Goeppert; Miklos Czaun; John-Paul Jones; Prakash, G. K. S.; A. Olah, G. Recycling of Carbon Dioxide to Methanol and Derived Products – Closing the Loop. *Chem. Soc. Rev.* **2014**, *43* (23), 7995–8048. https://doi.org/10.1039/C4CS00122B.

(11) Cheng, W.-H.; Richter, M. H.; Sullivan, I.; Larson, D. M.; Xiang, C.; Brunschwig, B. S.; Atwater, H. A. CO2 Reduction to CO with 19% Efficiency in a Solar-Driven Gas Diffusion Electrode Flow Cell under Outdoor Solar Illumination. *ACS Energy Lett.* **2020**, *25*, 470–476. https://doi.org/10.1021/ACSENERGYLETT.9B02576.

(12) Costentin, C.; Robert, M.; Savéant, J.-M.; Tatin, A. Efficient and Selective Molecular Catalyst for the CO_2-to-CO Electrochemical Conversion in Water. *Proc. Natl. Acad. Sci.* **2015**, *112* (22), 6882–6886. https://doi.org/10.1073/PNAS.1507063112.

(13) Beddington, J.; Williams, E. *Dealing with Carbon Dioxide at Scale*; National Academy of Sciences, 2017.

(14) Wu, H.-L.; Li, X.-B.; Tung, C.-H.; Wu, L.-Z. Semiconductor Quantum Dots: An Emerging Candidate for CO2 Photoreduction. *Adv. Mater.* **2019**, *31* (36), 1900709. https://doi.org/10.1002/ADMA.201900709.

(15) Kodaimati, M. S.; McClelland, K. P.; He, C.; Lian, S.; Jiang, Y.; Zhang, Z.; Weiss, E. A. Viewpoint: Challenges in Colloidal Photocatalysis and Some Strategies for Addressing Them. *Inorg. Chem.* **2018**, *57* (7), 3659–3670. https://doi.org/10.1021/ACS.INORGCHEM.7B03182.

(16) Andrews, J. L.; Santos, D. A.; Meyyappan, M.; Williams, R. S.; Banerjee, S. Building Brain-Inspired Logic Circuits from Dynamically Switchable Transition-Metal Oxides. *Trends in Chemistry*. Cell Press November 1, 2019, pp 711–726. https://doi.org/10.1016/j.trechm.2019.07.005.

(17) Parija, A.; Waetzig, G. R.; Andrews, J. L.; Banerjee, S. Traversing Energy Landscapes Away from Equilibrium: Strategies for Accessing and Utilizing Metastable Phase Space. *J. Phys. Chem. C* **2018**, *122* (45), 25709–25728. https://doi.org/10.1021/acs.jpcc.8b04622.

(18) De Jesus, L. R.; Andrews, J. L.; Parija, A.; Banerjee, S. Defining Diffusion Pathways in Intercalation Cathode Materials: Some Lessons from V_2O_5 on Directing Cation Traffic. *ACS Energy Lett.* **2018**, *3* (4), 915–931. https://doi.org/10.1021/acsenergylett.8b00156.

(19) Milleville, C. C.; Pelcher, K. E.; Sfeir, M. Y.; Banerjee, S.; Watson, D. F. Directional Charge Transfer Mediated by Mid-Gap States: A Transient Absorption Spectroscopy Study of CdSe Quantum Dot/β-Pb0.33V2O5 Heterostructures. *J. Phys. Chem. C* **2016**, *120* (9), 5221–5232. https://doi.org/10.1021/ACS.JPCC.6B00231.

(20) Pelcher, K. E.; Milleville, C. C.; Wangoh, L.; Cho, J.; Sheng, A.; Chauhan, S.; Sfeir, M. Y.; Piper, L. F. J. J.; Watson, D. F.; Banerjee, S. Programming Interfacial Energetic Offsets and Charge Transfer in B-Pb0.33V2O5/Quantum-Dot Heterostructures: Tuning Valence-Band Edges to Overlap with Midgap States. *J. Phys. Chem. C* **2016**, *120* (51), 28992–29001.

(21) Andrews, J. L.; Cho, J.; Wangoh, L.; Suwandaratne, N.; Sheng, A.; Chauhan, S.; Nieto, K.; Mohr, A.; Kadassery, K. J.; Popeil, M. R.; Thakur, P. K.; Sfeir, M.; Lacy, D. C.; Lee, T.; Zhang, P.; Watson, D. F.; Piper, L. F. J.; Banerjee, S. Hole Extraction by Design in Photocatalytic Architectures Interfacing CdSe Quantum Dots with Topochemically Stabilized Tin Vanadium Oxide. *J. Am. Chem. Soc.* **2018**, *140* (49), 17163–17174. https://doi.org/10.1021/jacs.8b09924.

(22) Cho, J.; Sheng, A.; Suwandaratne, N.; Wangoh, L.; Andrews, J. L.; Zhang, P.; Piper, L. F. J.; Watson, D. F.; Banerjee, S. The Middle Road Less Taken: Electronic-Structure-Inspired Design of Hybrid Photocatalytic Platforms for Solar Fuel Generation. *Acc. Chem. Res.* **2018**, *52* (3), 645–655. https://doi.org/10.1021/ACS.ACCOUNTS.8B00378.

(23) Kamat, P. V.; Christians, J. A.; Radich, E. J. Quantum Dot Solar Cells: Hole Transfer as a Limiting Factor in Boosting the Photoconversion Efficiency. *Langmuir* **2014**, *30* (20), 5716–5725. https://doi.org/10.1021/LA500555W.

(24) Spanhel, L.; Haase, M.; Weller, H.; Henglein, A. Photochemistry of Colloidal Semiconductors. 20. Surface Modification and Stability of Strong Luminescing CdS Particles. *J. Am. Chem. Soc.* **1987**, *109* (19), 5649–5655.

(25) Pelcher, K. E.; Milleville, C. C.; Wangoh, L.; Chauhan, S.; Crawley, M. R.; Marley, P. M.; Piper, L. F. J. J.; Watson, D. F.; Banerjee, S. Integrating B-Pb0.33V2O5 Nanowires with CdSe Quantum Dots: Toward Nanoscale Heterostructures with Tunable Interfacial Energetic Offsets for Charge Transfer. *Chem. Mater.* **2015**, *27* (7), 2468–2479.

(26) Jasieniak, J.; Califano, M.; Watkins, S. E. Size-Dependent Valence and Conduction Band-Edge Energies of Semiconductor Nanocrystals. *ACS Nano* **2011**, *5* (7), 5888–5902. https://doi.org/10.1021/NN201681S/SUPPL_FILE/NN201681S_SI_001.PDF.

(27) Lee, J. R. I.; Meulenberg, R. W.; Hanif, K. M.; Mattoussi, H.; Klepeis, J. E.; Terminello, L. J.; Van Buuren, T. Experimental Observation of Quantum Confinement in the Conduction Band of CdSe Quantum Dots. *Phys. Rev. Lett.* **2006**. *98* (14), 146803.

10.1103/PHYSREVLETT.98.146803/FIGURES/3/MEDIUM

(28) Oh, S. J.; Wang, Z.; Berry, N. E.; Choi, J. H.; Zhao, T.; Gaulding, E. A.; Paik, T.; Lai, Y.; Murray, C. B.; Kagan, C. R. Engineering Charge Injection and Charge Transport for High Performance PbSe Nanocrystal Thin Film Devices and Circuits. *Nano Lett.* **2014**, *14* (11), 6210–6216. https://doi.org/10.1021/NL502491D/SUPPL_FILE/NL502491D_SI_002.PDF.

(29) Chauhan, S.; Sheng, A.; Cho, J.; Razek, S. A.; Suwandaratne, N.; Sfeir, M. Y.; Piper, L. F. J.; Banerjee, S.; Watson, D. F. Type-II Heterostructures of α-V2O5 Nanowires Interfaced with Cadmium Chalcogenide Quantum Dots: Programmable Energetic Offsets, Ultrafast Charge Transfer, and Photocatalytic Hydrogen Evolution. *J. Chem. Phys.* **2019**, *151* (22), 224702. https://doi.org/10.1063/1.5128148.

(30) Cho, J.; Suwandaratne, N. S.; Razek, S.; Choi, Y.-H.; Piper, L. F. J.; Watson, D. F.; Banerjee, S. Elucidating the Mechanistic Origins of Photocatalytic Hydrogen Evolution Mediated by MoS2/CdS Quantum-Dot Heterostructures. *ACS Appl. Mater. Interfaces* **2020**, *12* (39), 43728–43740. https://doi.org/10.1021/ACSAMI.0C12583.

(31) Matthew W. Stoltzfus; Patrick M. Woodward, *; Ram Seshadri, †; Jae-Hyun Klepeis, ‡ and; Bursten§, B. Structure and Bonding in SnWO4, PbWO4, and BiVO4: Lone Pairs vs Inert Pairs. *Inorg. Chem.* **2007**, *46* (10), 3839–3850. https://doi.org/10.1021/IC061157G.

(32) Galy, J.; Meunier, G.; Andersson, S.; Åström, A. Stéréochimie Des Eléments Comportant Des Paires Non Liées: Ge (II), As (III), Se (IV), Br (V), Sn (II), Sb (III), Te (IV), I (V), Xe (VI), Tl (I), Pb (II), et Bi (III) (Oxydes, Fluorures et Oxyfluorures). *J. Solid State Chem.* **1975**, *13* (1–2), 142–159. https://doi.org/10.1016/0022-4596(75)90092-4.

(33) Liang, F.; Kang, L.; Lin, Z.; Wu, Y. Mid-Infrared Nonlinear Optical Materials Based on Metal Chalcogenides: Structure–Property Relationship. *Cryst. Growth Des.* **2017**, *17* (4), 2254–2289. https://doi.org/10.1021/ACS.CGD.7B00214.

(34) Dang, U.; Zaheer, W.; Zhou, W.; Kandel, A.; Orr, M.; Schwenz, R. W.; Laurita, G.; Banerjee, S.; Macaluso, R. T. Lattice Anharmonicity of Stereochemically Active Lone Pairs Controls Thermochromic Band Gap Reduction of $PbVO_3Cl$. *Chem. Mater.* **2020**, *32* (17), 7404–7412. https://doi.org/10.1021/ACS.CHEMMATER.0C02342.

(35) Wangoh, L.; Marley, P. M.; Quackenbush, N. F.; Sallis, S.; Fischer, D. A.; Woicik, J. C.; Banerjee, S.; Piper, L. F. J. Electron Lone Pair Distortion Facilitated Metal-Insulator Transition in β-$Pb_{0.33}V_2O_5$ Nanowires. *Appl. Phys. Lett.* **2014**, *104* (18), 182108. https://doi.org/10.1063/1.4875747.

(36) Marley, P. M.; Stabile, A. A.; Kwan, C. P.; Singh, S.; Zhang, P.; Sambandamurthy, G.; Banerjee, S. Charge Disproportionation and Voltage-Induced Metal-Insulator Transitions Evidenced in β-$Pb_xV_2O_5$ Nanowires. *Adv. Funct. Mater.* **2013**, *23* (2), 153–160. https://doi.org/10.1002/adfm.201201513.

(37) Fabini, D. H.; Laurita, G.; Bechtel, J. S.; Stoumpos, C. C.; Evans, H. A.; Kontos, A. G.; Raptis, Y. S.; Falaras, P.; Ven, A. Van der; Kanatzidis, M. G.; Seshadri, R. Dynamic Stereochemical Activity of the Sn2+ Lone Pair in Perovskite $CsSnBr_3$. *J. Am. Chem. Soc.* **2016**, *138* (36), 11820–11832. https://doi.org/10.1021/JACS.6B06287.

(38) Fabini, D. H.; Stoumpos, C. C.; Laurita, G.; Kaltzoglou, A.; Kontos, A. G.; Falaras, P.; Kanatzidis, M. G.; Seshadri, R. Reentrant Structural and Optical Properties and Large Positive Thermal Expansion in Perovskite Formamidinium Lead Iodide. *Angew. Chemie* **2016**, *128* (49), 15618–15622. https://doi.org/10.1002/ANGE.201609538.

(39) Zaheer, W.; Andrews, J. L.; Parija, A.; Hyler, F. P.; Jaye, C.; Weiland, C.; Yu, Y.-S.; Shapiro, D. A.; Fischer, D. A.; Guo, J.; Velázquez, J. M.; Banerjee, S. Reversible Room-Temperature Fluoride-Ion Insertion in a Tunnel-Structured Transition Metal Oxide Host. *ACS Energy Lett.* **2020**, *5* (8), 2520–2526. https://doi.org/10.1021/ACSENERGYLETT.0C01328.

(40) Zaheer, W.; Agbeworvi, G.; Perez-Beltran, S.; Andrews, J. L.; Aierken, Y.; Weiland, C.; Jaye, C.; Yu, Y.-S.; Shapiro, D. A.; Fakra, S. C.; Fischer, D. A.; Guo, J.; Prendergast, D.; Banerjee, S. Lessons Learned from $FeSb_2O_4$ on Stereoactive Lone Pairs as a Design Principle for Anion Insertion. *Cell Reports Phys. Sci.* **2021**, *2* (10), 100592. https://doi.org/10.1016/J.XCRP.2021.100592.

(41) Walsh, A.; Payne, D. J.; Egdell, R. G.; Watson, G. W. Stereochemistry of Post-Transition Metal Oxides: Revision of the Classical Lone Pair Model. *Chem. Soc. Rev.* **2011**, *40* (9), 4455–4463. https://doi.org/10.1039/c1cs15098g.

(42) Walsh, A.; Watson, G. W. The Origin of the Stereochemically Active Pb(II) Lone Pair: DFT Calculations on PbO and PbS. *J. Solid State Chem.* **2005**, *178* (5), 1422–1428. https://doi.org/10.1016/j.jssc.2005.01.030.

(43) Kalha, C.; Fernando, N. K.; Bhatt, P.; Johansson, F. O. L.; Lindblad, A.; Rensmo, H.; Medina, L. Z.; Lindblad, R.; Siol, S.; Jeurgens, L. P. H.; Cancellieri, C.; Rossnagel, K.; Medjanik, K.; Schönhense, G.; Simon, M.; Gray, A. X.; Nemšák, S.; Lömker, P.; Schlueter, C.; Regoutz, A. Hard X-Ray Photoelectron Spectroscopy: A Snapshot of the State-of-the-Art in 2020. *J. Phys. Condens. Matter* **2021**, *33* (23), 233001. https://doi.org/10.1088/1361-648X/ABEACD.

(44) Manikandan, M.; Tanabe, T.; Li, P.; Ueda, S.; Ramesh, G. V.; Kodiyath, R.; Wang, J.; Hara, T.; Dakshanamoorthy, A.; Ishihara, S.; Ariga, K.; Ye, J.; Umezawa, N.; Abe, H. Photocatalytic Water Splitting under Visible Light by Mixed-Valence Sn3O4. *ACS Appl. Mater. Interfaces* **2014**, *6* (6), 3790–3793. https://doi.org/10.1021/AM500157U.

(45) Kelaidis, N.; Bousiadi, S.; Zervos, M.; Chroneos, A.; Lathiotakis, N. N. Electronic Properties of the $Sn_{1-x}Pb_xO$ Alloy and Band Alignment of the SnO/PbO System: A DFT Study. *Sci. Reports 2020 101* **2020**, *10* (1), 1–8. https://doi.org/10.1038/s41598-020-73703-y.

(46) Sayama, K.; Nomura, A.; Zou, Z.; Abe, R.; Abe, Y.; Arakawa, H. Photoelectrochemical Decomposition of Water on Nanocrystalline $BiVO_4$ Film Electrodes under Visible Light. *Chem. Commun.* **2003**, *3* (23), 2908–2909. https://doi.org/10.1039/B310428A.

(47) Hermans, Y.; Murcia-López, S.; Klein, A.; Krol, R. van de; Andreu, T.; Morante, J. R.; Toupance, T.; Jaegermann, W. Analysis of the Interfacial Characteristics of $BiVO_4$/Metal Oxide Heterostructures and Its Implication on Their Junction Properties. *Phys. Chem. Chem. Phys.* **2019**, *21* (9), 5086–5096. https://doi.org/10.1039/C8CP07483F.

(48) Walsh, A.; Yan, Y.; Huda, M. N.; Al-Jassim, M. M.; Wei, S.-H. Band Edge Electronic Structure of BiVO4: Elucidating the Role of the Bi s and V d Orbitals. *Chem. Mater.* **2009**, *21* (3), 547–551. https://doi.org/10.1021/CM802894Z.

(49) Chang, X.; Wang, T.; Zhang, P.; Zhang, J.; Li, A.; Gong, J. Enhanced Surface Reaction Kinetics and Charge Separation of p–n Heterojunction Co3O4/BiVO4 Photoanodes. *J. Am. Chem. Soc.* **2015**, *137* (26), 8356–8359. https://doi.org/10.1021/JACS.5B04186.

(50) Jun, H. K.; Careem, M. A.; Arof, A. K. Quantum Dot-Sensitized Solar Cells—Perspective and Recent Developments: A Review of Cd Chalcogenide Quantum Dots as Sensitizers. *Renew. Sustain. Energy Rev.* **2013**, *22*, 148–167. https://doi.org/10.1016/J.RSER.2013.01.030.

(51) Zavalij, P. Y.; Whittingham, M. S. Structural Chemistry of Vanadium Oxides with Open Frameworks. *Acta Crystallogr.* **1999**, *B55*, 627–663. https://doi.org/10.1107/S0108768199004000.

(52) Galy, J. Vanadium Pentoxide and Vanadium Oxide Bronzes - Structural Chemistry of Single (S) and Double (D) Layer $M_xV_2O_5$ Phases. *J. Solid State Chem.* **1992**, *100* (2), 229–245. https://doi.org/10.1016/0022-4596(92)90097-F.

(53) Inomata, Y.; Hata, S.; Mino, M.; Kiyonaga, E.; Morita, K.; Hikino, K.; Yoshida, K.; Kubota, H.; Toyao, T.; Shimizu, K. I.; Haruta, M.; Murayama, T. Bulk Vanadium Oxide versus Conventional V_2O_5/TiO_2: NH_3-SCR Catalysts Working at a Low Temperature below 150 °C. *ACS Catal.* **2019**, *9* (10), 9327–9331. https://doi.org/10.1021/ACSCATAL.9B02695/SUPPL_FILE/CS9B02695_SI_001.PDF.

(54) Marley, P. M.; Horrocks, G. A.; Pelcher, K. E.; Banerjee, S. Transformers: The Changing Phases of Low-Dimensional Vanadium Oxide Bronzes. *Chem. Commun.* **2015**, *51* (25), 5181–5198. https://doi.org/10.1039/C4CC08673B.

(55) Marley, P. M.; Abtew, T. A.; Farley, K. E.; Horrocks, G. A.; Dennis, R. V.; Zhang, P.; Banerjee, S. Emptying and Filling a Tunnel Bronze. *Chem. Sci.* **2015**, *6* (3), 1712–1718. https://doi.org/10.1039/C4SC03748K.

(56) Parija, A.; Handy, J. V.; Andrews, J. L.; Wu, J.; Wangoh, L.; Singh, S.; Jozwiak, C.; Bostwick, A.; Rotenberg, E.; Yang, W.; Fakra, S. C.; Al-Hashimi, M.; Sambandamurthy, G.; Piper, L. F. J.; Williams, R. S.; Prendergast, D.; Banerjee, S. Metal-Insulator Transitions in B′-CuxV2O5 Mediated by Polaron Oscillation and Cation Shuttling. *Matter* **2020**, *2* (5), 1166–1186. https://doi.org/10.1016/J.MATT.2020.01.027.

(57) Handy, J. V.; Luo, Y.; Andrews, J. L.; Bhuvanesh, N.; Banerjee, S. An Atomic View of Cation Diffusion Pathways from Single-Crystal Topochemical Transformations. *Angew. Chemie Int. Ed.* **2020**, *59* (38), anie.202005513. https://doi.org/10.1002/anie.202005513.

(58) Withers, R. L.; Millet, P.; Tabira, Y. The Inherent Displacive Structural Flexibility of MxV2O5 Framework Structures. *Zeitschrift für Krist. - Cryst. Mater.* **2000**, *215* (6), 357–363. https://doi.org/10.1524/ZKRI.2000.215.6.357.

(59) Gautam, G. S.; Canepa, P.; Malik, R.; Liu, M.; Persson, K.; Ceder, G. First-Principles Evaluation of Multi-Valent Cation Insertion into Orthorhombic V_2O_5. *Chem. Commun.*

2015, *51* (71), 13619–13622. https://doi.org/10.1039/C5CC04947D.

(60) Galy, J. Vanadium Pentoxide and Vanadium Oxide Bronzes-Structural Chemistry of Single (S) and Double (D) Layer MxV2O5 Phases. *J. Solid State Chem.* **1992**, *100* (2), 229–245. https://doi.org/10.1016/0022-4596(92)90097-F.

(61) Rong, Z.; Malik, R.; Canepa, P.; Sai Gautam, G.; Liu, M.; Jain, A.; Persson, K.; Ceder, G. Materials Design Rules for Multivalention Mobility in Intercalation Structures. *Chem. Mater.* **2015**, *27* (17), 6016–6021. https://doi.org/10.1021/acs.chemmater.5b02342.

(62) Hu, W.; Du, X.; Wu, Y.; Wang, L. Novel ε-$Cu_{0.95}V_2O_5$ Hollow Microspheres and α-CuV_2O_5 Nanograins: Facile Synthesis and Application in Lithium-Ion Batteries. *J. Power Sources* **2013**, *237*, 112–118. https://doi.org/10.1016/j.jpowsour.2013.03.002.

(63) Oka, Y.; Yao, T.; Yamamoto, N. Crystal Structures of Hydrated Vanadium Oxides Withδ-Type V2O5Layers:δ-$M_{0.25}V_2O_5{\cdot}H_2O$,M=Ca, Ni. *J. Solid State Chem.* **1997**, *132* (2), 323–329. https://doi.org/10.1006/JSSC.1997.7467.

(64) Oka, Y.; Yao, T.; Yamamoto, N. Crystal Structures and Lattice Distortions Ofσ-Type Layered Vanadium Bronzes:σ-$M_{0.25}V_2O_5{\cdot}H_2O$ (M=Mg, Co, Ni). *J. Solid State Chem.* **1999**, *144* (1), 181–187. https://doi.org/10.1006/JSSC.1999.8155.

(65) Marley, P. M.; Singh, S.; Abtew, T. A.; Jaye, C.; Fischer, D. A.; Zhang, P.; Sambandamurthy, G.; Banerjee, S. Electronic Phase Transitions of δ-$Ag_xV_2O_5$ Nanowires: Interplay between Geometric and Electronic Structures. *J. Phys. Chem. C* **2014**, *118* (36), 21235–21243. https://doi.org/10.1021/JP506238S.

(66) Ganne, M.; Jouanneaux, A.; Tournoux, M.; Le Bail, A. Structure and Phase Transitions of Low-Dimensional Thallium Vanadium Bronze $Tl_xV_2O_5$ ($0.44 \leq x \leq 0.48$). *J. Solid State Chem.* **1992**, *97* (1), 186–198. https://doi.org/10.1016/0022-4596(92)90024-P.

(67) Ballone, P.; Galli, G. Bonding Properties of Mercury Dimers in the Pseudopotential Local-Density-Approximation Scheme. *Phys. Rev. B* **1989**, *40* (12), 8563. https://doi.org/10.1103/PhysRevB.40.8563.

(68) Hermes, W.; Dollé, M.; Rozier, P.; Lidin, S. The Composite Structure of Mixed τ-$(Ag, Cu)_xV_2O_5$ Bronzes—Evidence for T Dependant Guest-Species Ordering and Mobility. *J. Solid State Chem.* **2013**, *199*, 84–89. https://doi.org/10.1016/j.jssc.2012.11.029.

(69) Pecquenard, B.; Zavalij, P. Y.; Whittingham, M. S. Tetrakis(Tetramethylammonium) Dihydrogendecavanadate Acetic Acid 2.8-Hydrate, $[N(CH_3)_4]_4[H_2V_{10}O_{28}].CH_3COOH.2.8H_2O$. *urn:issn:0108-2701* **1998**, *54* (12), 1833–1835. https://doi.org/10.1107/S0108270198009044.

(70) Dong, B.; Gómez-García, C. J.; Peng, J.; Benmansour, S.; Ma, J. A Novel Oxovanadate Structural Type – Synthesis, Single Crystal Structure and Magnetic Properties of a Mixed-Valence Polyoxovanadate Formed by $\{V_{17}O_{40}(Cl)\}$ and $\{V_{15}O_{36}(Cl)\}$ Clusters. *Polyhedron* **2007**, *26* (6), 1310–1316. https://doi.org/10.1016/J.POLY.2006.10.050.

(71) Jabor, J. K.; Stößer, R.; Thong, N. H.; Ziemer, B.; Meisel, M. Unexpected Reactions of $[Ag(NCCH_3)_3][(V_2O_3)_2(RPO_3)_4{\subset}F]$ Cage Compounds with H_2 and NO. *Angew. Chemie*

Int. Ed. **2007**, *46* (33), 6354–6356. https://doi.org/10.1002/ANIE.200701211.

(72) Hong, S.; Burkhow, S. J.; Doughty, R. M.; Cheng, Y.; Ryan, B. J.; Mantravadi, A.; Roling, L. T.; Panthani, M. G.; Osterloh, F. E.; Smith, E. A.; Zaikina, J. V. Local Structural Disorder in Metavanadates MV_2O_6 (M = Zn and Cu) Synthesized by the Deep Eutectic Solvent Route: Photoactive Oxides with Oxygen Vacancies. *Chem. Mater.* **2021**, *33* (5), 1667–1682. https://doi.org/10.1021/ACS.CHEMMATER.0C04155.

(73) Yan, B.; Maggard, P. A. M(Bipyridine)V_4O_{10} (M = Cu, Ag): Hybrid Analogues of Low-Dimensional Reduced Vanadates. *Inorg. Chem.* **2007**, *46* (16), 6640–6646. https://doi.org/10.1021/ic700729q.

(74) Nadia Marino; Francisco Lloret; Miguel Julve; P. Doyle, R. Synthetically Persistent, Self Assembled [V IV 2 V V 4] Polyoxovanadates: Facile Synthesis, Structure and Magnetic Analysis. *Dalt. Trans.* **2011**, *40* (45), 12248–12256. https://doi.org/10.1039/C1DT11004G.

(75) Yang, H.; Li, J.; Zhang, X. gang; Jin, Y. li. Synthesis of LiV3O8 Nanocrystallites as Cathode Materials for Lithium Ion Batteries. *J. Mater. Process. Technol.* **2008**, *207* (1–3), 265–270. https://doi.org/10.1016/J.JMATPROTEC.2007.12.122.

(76) Guicun Li, *; Shuping Pang; Li Jiang; Zhiyan Guo, and; Zhang, Z. Environmentally Friendly Chemical Route to Vanadium Oxide Single-Crystalline Nanobelts as a Cathode Material for Lithium-Ion Batteries. *J. Phys. Chem. B* **2006**, *110* (19), 9383–9386. https://doi.org/10.1021/JP060904S.

(77) Evans, H. T.; Block, S. The Crystal Structures of Potassium and Cesium Trivanadates. *Inorg. Chem.* **1966**, *5* (10), 1808–1814.

(78) Oka, Y.; Yao, T.; Yamamoto, N. Hydrothermal Synthesis and Structure Refinements of Alkali-Metal Trivanadates AV_3O_8 (A = K, Rb, Cs). *Mater. Res. Bull.* **1997**, *32* (9), 1201–1209. https://doi.org/10.1016/S0025-5408(97)00096-2.

(79) Suzuki, H.; Kunioku, H.; Higashi, M.; Tomita, O.; Kato, D.; Kageyama, H.; Abe, R. Lead Bismuth Oxyhalides $PbBiO_2X$ (X = Cl, Br) as Visible-Light-Responsive Photocatalysts for Water Oxidation: Role of Lone-Pair Electrons in Valence Band Engineering. *Chem. Mater.* **2018**, *30* (17), 5862–5869. https://doi.org/10.1021/ACS.CHEMMATER.8B01385.

(80) Yungi Lee, †; Hiroaki Terashima, ‡; Yoshiki Shimodaira, §; Kentaro Teramura, †; Michikazu Hara, ‡; Hisayoshi Kobayashi, ∥; Kazunari Domen, *,†,⊥ and; Yashima∞, M. Zinc Germanium Oxynitride as a Photocatalyst for Overall Water Splitting under Visible Light. *J. Phys. Chem. C* **2006**, *111* (2), 1042–1048. https://doi.org/10.1021/JP0656532.

(81) Akio Ishikawa, †; Tsuyoshi Takata, †; Junko N. Kondo, †; Michikazu Hara, †; Hisayoshi Kobayashi, ‡ and; Kazunari Domen*, §. Oxysulfide Sm2Ti2S2O5 as a Stable Photocatalyst for Water Oxidation and Reduction under Visible Light Irradiation ($\lambda \leq 650$ Nm). *J. Am. Chem. Soc.* **2002**, *124* (45), 13547–13553. https://doi.org/10.1021/JA0269643.

(82) Jianwei Sun; K. Zhong, D.; R. Gamelin, D. Composite Photoanodes for Photoelectrochemical Solar Water Splitting. *Energy Environ. Sci.* **2010**, *3* (9), 1252–1261.

https://doi.org/10.1039/C0EE00030B.

(83) Gary Hodes. Semiconductor and Ceramic Nanoparticle Films Deposited by Chemical Bath Deposition. *Phys. Chem. Chem. Phys.* **2007**, *9* (18), 2181–2196. https://doi.org/10.1039/B616684A.

(84) Hone, F.; Abza, T. Short Review of Factors Affecting Chemical Bath Deposition Method for Metal Chalcogenide Thin Films. *Int. J. Thin Film. Sci. Technol.* **2019**, *8* (2), 43–53.

(85) Wang, W.; Jiang, G.; Yu, J.; Wang, W.; Pan, Z.; Nakazawa, N.; Shen, Q.; Zhong, X. High Efficiency Quantum Dot Sensitized Solar Cells Based on Direct Adsorption of Quantum Dots on Photoanodes. *ACS Appl. Mater. Interfaces* **2017**, *9* (27), 22549–22559. https://doi.org/10.1021/ACSAMI.7B05598.

(86) Mohamed Mustakim, N. S.; Ubani, C. A.; Sepeai, S.; Ahmad Ludin, N.; Mat Teridi, M. A.; Ibrahim, M. A. Quantum Dots Processed by SILAR for Solar Cell Applications. *Sol. Energy* **2018**, *163*, 256–270. https://doi.org/10.1016/J.SOLENER.2018.02.003.

(87) Pathan, H. M.; Lokhande, C. D. Deposition of Metal Chalcogenide Thin Films by Successive Ionic Layer Adsorption and Reaction (SILAR) Method. *Bull. Mater. Sci. 2004 272* **2004**, *27* (2), 85–111. https://doi.org/10.1007/BF02708491.

(88) Watson, D. F. Linker-Assisted Assembly and Interfacial Electron-Transfer Reactivity of Quantum Dot−Substrate Architectures. *J. Phys. Chem. Lett.* **2010**, *1* (15), 2299–2309. https://doi.org/10.1021/JZ100571U.

(89) Cheng, K.; Wang, H.; Bang, J.; West, D.; Zhao, J.; Zhang, S. Carrier Dynamics and Transfer across the CdS/MoS_2 Interface upon Optical Excitation. *J. Phys. Chem. Lett.* **2020**, *11* (16), 6544–6550. https://doi.org/10.1021/ACS.JPCLETT.0C01188.

(90) S. Selinsky, R.; Qi Ding; S. Faber, M.; C. Wright, J.; Song Jin. Quantum Dot Nanoscale Heterostructures for Solar Energy Conversion. *Chem. Soc. Rev.* **2013**, *42* (7), 2963–2985. https://doi.org/10.1039/C2CS35374A.

(91) Park, C.; Ding, Y. *Data Science for Nano Image Analysis*; Springer, 2021.

(92) Weiland, C.; Rumaiz, A. K.; Pianetta, P.; Woicik, J. C. Recent Applications of Hard X-Ray Photoelectron Spectroscopy. *J. Vac. Sci. Technol. A Vacuum, Surfaces, Film.* **2016**, *34* (3), 030801. https://doi.org/10.1116/1.4946046.

(93) Sakata, T.; Hashimoto, K.; Hiramoto, M. New Aspects of Electron Transfer on Semiconductor Surface: Dye-Sensitization System. *J. Phys. Chem.* **1990**, *94* (7), 3040–3045.

(94) Tvrdy, K.; Frantsuzov, P. A.; Kamat, P. V. Photoinduced Electron Transfer from Semiconductor Quantum Dots to Metal Oxide Nanoparticles. *Proc. Natl. Acad. Sci.* **2011**, *108* (1), 29–34. https://doi.org/10.1073/PNAS.1011972107.

(95) Braham, E. J.; Davidson, R. D.; Mohammed Al-Hashimi; Raymundo Arróyave; Sarbajit Banerjee. Navigating the Design Space of Inorganic Materials Synthesis Using Statistical Methods and Machine Learning. *Dalt. Trans.* **2020**, *49* (33), 11480–11488. https://doi.org/10.1039/D0DT02028A.

(96) Adamson, D.; Deligkas, A.; Gusev, V. V.; Potapov, I. On the Hardness of Energy Minimisation for Crystal Structure Prediction. *Lect. Notes Comput. Sci. (including Subser. Lect. Notes Artif. Intell. Lect. Notes Bioinformatics)* **2020**, *12011 LNCS*, 587–596. https://doi.org/10.1007/978-3-030-38919-2_48.

(97) Sun, W.; Dacek, S. T.; Ong, S. P.; Hautier, G.; Jain, A.; Richards, W. D.; Gamst, A. C.; Persson, K. A.; Ceder, G. The Thermodynamic Scale of Inorganic Crystalline Metastability. *Sci. Adv.* **2016**, *2* (11), e1600225. https://doi.org/10.1126/sciadv.1600225.

(98) Navrotsky, A. Nanoscale Effects on Thermodynamics and Phase Equilibria in Oxide Systems. *ChemPhysChem* **2011**, *12* (12), 2207–2215. https://doi.org/10.1002/CPHC.201100129.

(99) Ahmed, I.; Galoppo, T.; Hu, X.; Ding, Y. Graph Regularized Autoencoder and Its Application in Unsupervised Anomaly Detection. *IEEE Trans. Pattern Anal. Mach. Intell.* **2020**, *XX*, 1.

(100) Wang, J.; Xia, T.; Wang, L.; Zheng, X.; Qi, Z.; Gao, C.; Zhu, J.; Li, Z.; Xu, H.; Xiong, Y. Enabling Visible-Light-Driven Selective CO_2 Reduction by Doping Quantum Dots: Trapping Electrons and Suppressing H_2 Evolution. *Angew. Chemie Int. Ed.* **2018**, *57* (50), 16447–16451. https://doi.org/10.1002/ANIE.201810550.

(101) Kuehnel, M. F.; Orchard, K. L.; Dalle, K. E.; Reisner, E. Selective Photocatalytic CO_2 Reduction in Water through Anchoring of a Molecular Ni Catalyst on CdS Nanocrystals. *J. Am. Chem. Soc.* **2017**, *139* (21), 7217–7223. https://doi.org/10.1021/JACS.7B00369.

(102) Bi, Q.-Q.; Wang, J.-W.; Lv, J.-X.; Wang, J.; Zhang, W.; Lu, T.-B. Selective Photocatalytic CO_2 Reduction in Water by Electrostatic Assembly of CdS Nanocrystals with a Dinuclear Cobalt Catalyst. *ACS Catal.* **2018**, *8* (12), 11815–11821. https://doi.org/10.1021/ACSCATAL.8B03457.

(103) Lian, S.; Kodaimati, M. S.; Dolzhnikov, D. S.; Calzada, R.; Weiss, E. A. Powering a CO_2 Reduction Catalyst with Visible Light through Multiple Sub-Picosecond Electron Transfers from a Quantum Dot. *J. Am. Chem. Soc.* **2017**, *139* (26), 8931–8938. https://doi.org/10.1021/JACS.7B03134.

(104) Lian, S.; Kodaimati, M. S.; Weiss, E. A. Photocatalytically Active Superstructures of Quantum Dots and Iron Porphyrins for Reduction of CO_2 to CO in Water. *ACS Nano* **2018**, *12* (1), 568–575. https://doi.org/10.1021/ACSNANO.7B07377.

(105) Asadi, M.; Kumar, B.; Behranginia, A.; Rosen, B. A.; Baskin, A.; Repnin, N.; Pisasale, D.; Phillips, P.; Zhu, W.; Haasch, R.; Klie, R. F.; Král, P.; Abiade, J.; Salehi-Khojin, A. Robust Carbon Dioxide Reduction on Molybdenum Disulphide Edges. *Nat. Commun. 2014 51* **2014**, *5* (1), 1–8. https://doi.org/10.1038/ncomms5470.

(106) Asadi, M.; Kim, K.; Liu, C.; Addepalli, A. V.; Abbasi, P.; Yasaei, P.; Phillips, P.; Behranginia, A.; Cerrato, J. M.; Haasch, R.; Zapol, P.; Kumar, B.; Klie, R. F.; Abiade, J.; Curtiss, L. A.; Salehi-Khojin, A. Nanostructured Transition Metal Dichalcogenide Electrocatalysts for CO2 Reduction in Ionic Liquid. *Science (80-.).* **2016**, *353* (6298), 467–470. https://doi.org/10.1126/SCIENCE.AAF4767.

(107) Xu, J.; Li, X.; Liu, W.; Sun, Y.; Ju, Z.; Yao, T.; Wang, C.; Ju, H.; Zhu, J.; Wei, S.; Xie, Y. Carbon Dioxide Electroreduction into Syngas Boosted by a Partially Delocalized Charge in Molybdenum Sulfide Selenide Alloy Monolayers. *Angew. Chemie Int. Ed.* **2017**, *56* (31), 9121–9125. https://doi.org/10.1002/ANIE.201704928.

(108) Perryman, J. T.; Velázquez, J. M. Design Principles for Multinary Metal Chalcogenides: Toward Programmable Reactivity in Energy Conversion†. *Chem. Mater.* **2021**, *33* (18), 7133–7147. https://doi.org/10.1021/ACS.CHEMMATER.1C01983.

(109) T. Perryman, J.; C. Ortiz-Rodríguez, J.; W. Jude, J.; P. Hyler, F.; C. Davis, R.; Apurva Mehta; R. Kulkarni, A.; J. Patridge, C.; M. Velázquez, J. Metal-Promoted Mo 6 S 8 Clusters: A Platform for Probing Ensemble Effects on the Electrochemical Conversion of CO 2 and CO to Methanol. *Mater. Horizons* **2020**, *7* (1), 193–202. https://doi.org/10.1039/C9MH00745H.

(110) Li, A.; Wang, T.; Li, C.; Huang, Z.; Luo, Z.; Gong, J. Adjusting the Reduction Potential of Electrons by Quantum Confinement for Selective Photoreduction of CO2 to Methanol. *Angew. Chemie Int. Ed.* **2019**, *58* (12), 3804–3808. https://doi.org/10.1002/ANIE.201812773.

(111) Zhao, J.; Holmes, M. A.; Osterloh, F. E. Quantum Confinement Controls Photocatalysis: A Free Energy Analysis for Photocatalytic Proton Reduction at CdSe Nanocrystals. *ACS Nano* **2013**, *7* (5), 4316–4325. https://doi.org/10.1021/NN400826H.

(112) Jiang, Y.; Yang, M.; Wu, Y.; López-Arteaga, R.; Rogers, C. R.; Weiss, E. A. Chemo- and Stereoselective Intermolecular [2 + 2] Photocycloaddition of Conjugated Dienes Using Colloidal Nanocrystal Photocatalysts. *Chem Catal.* **2021**, *1* (1), 106–116. https://doi.org/10.1016/J.CHECAT.2021.02.001.

(113) McClelland, K. P.; Clemons, T. D.; Stupp, S. I.; Weiss, E. A. Semiconductor Quantum Dots Are Efficient and Recyclable Photocatalysts for Aqueous PET-RAFT Polymerization. *ACS Macro Lett.* **2019**, *9* (1), 7–13. https://doi.org/10.1021/ACSMACROLETT.9B00891.

(114) Caputo, J. A.; Frenette, L. C.; Zhao, N.; Sowers, K. L.; Krauss, T. D.; Weix, D. J. General and Efficient C–C Bond Forming Photoredox Catalysis with Semiconductor Quantum Dots. *J. Am. Chem. Soc.* **2017**, *139* (12), 4250–4253. https://doi.org/10.1021/JACS.6B13379.

(115) Weiss, E. A. Designing the Surfaces of Semiconductor Quantum Dots for Colloidal Photocatalysis. *ACS Energy Lett.* **2017**, *2* (5), 1005–1013. https://doi.org/10.1021/ACSENERGYLETT.7B00061.

TOC Graphic

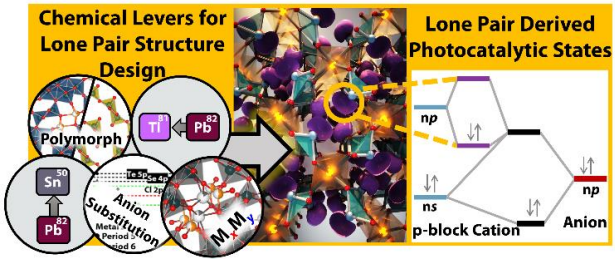
Chemical Levers for Lone Pair Structure Design
Polymorph
Tl
Pb
Sn
Pb
Anion Substitution
Metal
Period 5
Period 6
Lone Pair Derived Photocatalytic States
np
ns
np
p-block Cation
Anion